Understanding the fracture behavior of brittle and ductile multi-flawed rocks by uniaxial loading by digital image correlation

X.P.Zhou[ab]Y.J.Lian[ab]L.N.Y.Wong[c]F.Berto[d]

Abstract

Fracturing behavior of ductile multi-flawed rock mass is very different from those of brittle multi-flawed rock mass. However, there is a very vague distinction of the fracture mechanism of ductile multi-flawed rock mass from that of brittle multi-flawed rock mass due to the absence of quality experimental data. To evaluate the fracturing behavior and further reveal the failure mechanism of brittle and ductile multi-flawed rock masses, a comparison study on brittle and ductile laboratory rock-like specimens that contain nine pre-existing flaws subjected to uniaxial compression is conducted. The advanced optical technique, Digital Image Correlation (DIC), is adopted to capture the real-time displacement and strain fields on the surface of the rock-like specimens. The fractal dimension estimation method is introduced to quantitatively track the fracture process. The fracture process, the crack coalescence mode and the fracturing mechanism are obtained as well as the stress-strain response. For ductile multi-flawed rock-like specimens, four crack initiation modes and nine types of crack coalescence are observed. For brittle multi-flawed rock like specimens, four crack initiation modes and eight types of crack coalescence are observed. Comparison of fracturing behavior indicates that crack initiation mode transforms from shear crack to tensile crack as the brittleness index increases; the coalescence mode transforms from shear crack coalescence to the coalescence of tensile crack and shear crack; then to the tensile crack coalescence as the brittleness index increases. Observations on the ultimate failure modes indicate that the failure mode transforms from shear failure to the mixed tension-shear failure, then to splitting failure as the brittleness index increases. Most macrocracks in brittle multi-flawed rock-like specimens develop from crack coalescence occurring in a "columnar" pattern, while most macrocracks in ductile multi-flawed rock-like specimens develop from shear cracks. Moreover, the effects of the brittleness index on the complete stress-strain curve, the crack initiation stress and the peak strength are also investigated in detail.

Keywords

Fracturing behavior
Brittle–ductile transition
Multi-flawed specimens
Comparative study
DIC

1. Introduction

Fracturing behavior of multi-flawed rock mass is of the fundamental interest and importance for practical rock engineering, such as tunneling, mining, and blasting [1], [2], [3], [4]. Rock masses are complex geological mediums with multiple cracks, joints and faults, which strongly affect the performance of engineering structures in the rock masses. Such primary discontinuities in natural rocks are a source of initiation of new cracks. Under the actions of external engineering forces [5], new cracks may grow along all the possible directions and coalesce with primary fractures or other new cracks, which leads to the nonlinear degradation of the strength and the stiffness of rocks [6], [7]. Therefore, knowledge of the fracturing behavior of multi-flawed rock mass is necessary to accurately interpret and predict rock deformation behavior. Many experimental and theoretical studies were conducted to investigate fracturing behavior in brittle flawed rocks or rock-like materials under uniaxial compression [2], [3], [5], [7], [8], [9], [10], [11], [12], [13]. The core problem is the mechanism of crack growth under compressive loads. These previous studies indicated that fracturing behavior and failure mechanisms depend strongly on the orientation, spacing, continuity, in particular the amount of the flaws. The fracturing behavior in rocks or rock-like specimens containing multiple pre-existing flaws are obviously more complex than those containing one, two or three flaws. For example, five types of cracks, including wing cracks, quasi-coplanar secondary cracks, oblique secondary cracks, out-of-plane tensile cracks and out-of-plane shear cracks, along with ten types of crack coalescence created through the above five types of cracks were reported by Zhou et al. [3], who carried out the uniaxial compression tests on rock-like materials containing four pre-existing flaws. For another example, a number of uniaxial compression tests were conducted on specimens made of gypsum with 16 flaws by Sagong and Bobet [14]. As reported by Sagong and Bobet [14], nine types of crack coalescence can be observable, and each type of crack coalescence is characteristic of a particular flaw geometry. Moreover, the following types of coalescence cracks were identified by Afolagboye et al. [15]: primary tensile coalescence crack, tensile crack

linkage, shear crack linkage, mixed tensile-shear crack, and indirect crack coalescence. With reference to the experimental observation of crack initiation and propagation from pre-existing flaws in rock specimens under compression, the influences of pre-existing flaw inclination angle on the cracking processes were analyzed by means of finite element method (FEM) and non-linear dynamics method by Li and Wong [10]. A micro-mechanical based numerical manifold method (NMM) is proposed to investigate the micro-mechanisms underlying rock macroscopic fracture processes [16]. It was reported that with the increase of the contact stiffness ratio, the failure mode of rock under uniaxial compression transforms from a diffuse pattern to a concentrated shear band [16]. It is worth noting that a coupled experimental-numerical study was conducted by Zhang et al. [17] to investigate the quasi-static cracking behaviors and the underlying fracture mechanism of double-flawed rock-like specimens under uniaxial compressive loads. Three typical arrays of double pre-existing flaws, namely, the coplanar array, the vertical non-overlapping array and the vertical aligning array, are analyzed experimentally and numerically where the advanced peridynamics numerical tool was adopted [17]. In addition, the mechanical and fracturing behavior of rock mass is also affected by temperature and water, e.g., the thermal cracking for the former [18], [19], [20]and the hydraulic fracturing for the latter [21], [22]. These previous studies provide a good understanding of fracturing behavior and failure mechanisms in rock masses.

Note that most of previous studies focused on brittle rocks or rock-like materials [5], [13], [23], [24], [25], [26], [27], [28]. Natural rocks, however, may exhibit a significant ductility under various engineering conditions, e.g., rock mass surrounding the deep excavationswhere the in-situ stress is sufficiently large [29]. For deep underground engineering, the ductility of multi-flawed rock mass plays the decisive role in its ultimate fracturing patterns, as depicted in Fig. 1. Therefore, it may be inferred that cracking processes and cracking patterns for ductile multi-flawed rock masses differ much or even radically from those for brittle ones. Taking carbonate rocks as examples, brittle deformation of carbonate rocks is cataclastic in nature, where its deformation involves microcrack formation and frictional sliding along grain boundaries, whereas ductile deformation (at low temperature) transits to delocalized cataclasis (or ''cataclastic flow'') [30]. Also, as ductile deformation increases, pore collapse begins to play a more significant role than microcracking, leading to an initially compact stage in porous carbonate rock deformation (although this compact behavior ultimately transits to dilatant behavior at very large strains) [31]. Up to date, the fracturing behavior of ductile rocks or rock-like materials are rarely studied experimentally. Due to the

absence of experimental data, the effects of the ductility on fracturing behavior in multi-flawed rocks or rock-like specimens are unclear, which leads to the very vague distinction of the failure mechanism of ductile multi-flawed rocks or rock-like specimens from that of brittle ones. Note that a series of extensive uniaxial and triaxial compression tests were performed on Indiana Limestone by Walton et al. [30] to evaluate its post-yield mechanical and dilatational behavior across the brittle–ductile transition. Particular attention was paid to the post-yield evolution of strength and dilatancy, rather than the fracturing behavior and failure mechanisms.
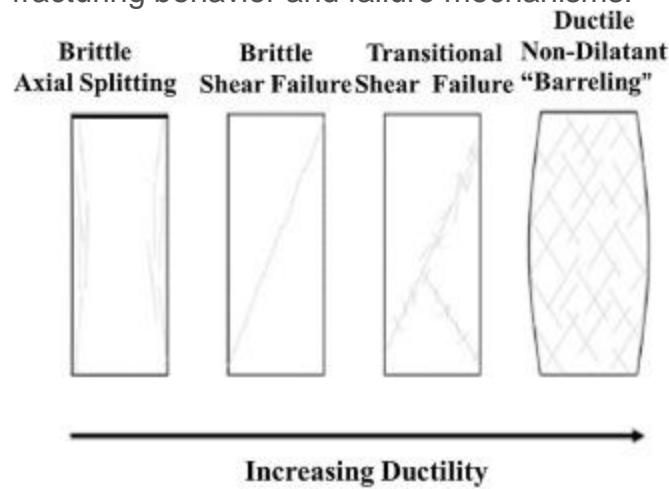
1. Download high-res image (109KB)
2. Download full-size image

Fig. 1. Schematic illustrating changes in failure patterns versus ductility [30].

To evaluate the fracturing behavior and further reveal the failure mechanism of multi-flawed rock masses across the brittle–ductile transition, this paper designs a comparison study by conducting the uniaxial compression tests on rock-like specimens made of two kind of mixture, as an attempt to represent the brittle rocks and ductile rocks. Each rock-like specimen contains nine pre-existing flaws. The advanced optical technique, digital specklecorrelation method (DSCM) or Digital Image Correlation (DIC), is adopted to capture the surface deformation of rock-like specimens. A fractal dimension estimation method is introduced to quantitatively track the fracture process. The present experimental studies mainly focus on the fracturing processes, the fracture patterns and the crack coalescence mechanism. The comparison study in this paper aims at providing the clear distinction of the fracturing behavior of ductile multi-flawed rock masses from that of brittle ones, and improving the understanding of the failure mechanism of rock-like specimens across the brittle–ductile transition.

This paper is organized as follows: the experimental setup is presented in Section 2. Axial stress-strain curve and crack initiation, propagation and coalescence are discussed in the Section 3. Initiation mode, initiation stress, coalescence mode and coalescence stress, are revealed by DSCM and ultimate failure mode are investigated in Section 4. Fracture process observed by fractal dimension method is introduced in Section 5. Conclusions are drawn in Section 6.

2. Specimen preparation and test system

2.1. Specimen preparation

The mechanism property of rock-like specimen largely depends on the mixture and its mass ratio. Only a proper content of mixture with a suitable mass ratio enables the specimens to contain the characteristics of rocks. Fortunately, content of mixture and reasonable mass ratio have been successfully investigated already. A mixture of barite, sand, plaster and water with a mass ratio of 2:4:1:1.5 is adopted to conduct rock-like specimens by Wong and Chau [31]. Wang and Chau concluded that the material is appropriate as a sandstone-like modelling material. In addition, the same mixture of barite, sand, plaster and water, but with different mass ratio of 126:9:9:16 was also used by Zhou and Cheng [3] to build Chongqing sandstone-like specimens for the fracture behavior study. Specimens conducted by the mass ratios mentioned above can achieve various peak strength, but share reasonable rock characteristics. In spite of this, according to the experimental result, low brittleness index, represents a ductility property of the specimens, cannot be successfully reached using this sort of mixture whatever mass ratios are adopted. Several attempts have been made to look for a new mixture, which can enable the specimens to earn a low brittleness index. When epoxy resin and polyamide are adopted to replace plaster in the mixture, ductile specimens are successfully conducted. Meanwhile, for a more effective productivity of specimens, alcohol is used in the mixture as well.

Thus, a mixture of sand, barite, epoxy resin, polyamide and alcohol with various mass ratios is used to conduct ductile rock-like material specimens, as shown in Table 1. A mixture of sand, barite, colophony and alcohol with various mass ratios is adopted to build brittle specimens, as shown in Table 2.

Table 1. Proportion of ductile material.

Number	Mixture	Mass ratio
A1,A2,A3,A4	Sand: Barite: Epoxy resin: Polyamide: Alcohol	300:300:4:4:51
B1,B2,B3,B4	Sand: Barite: Epoxy resin: Polyamide: Alcohol	300:300:6:6:51

Number	Mixture	Mass ratio
C1,C2,C3,C4	Sand: Barite: Epoxy resin: Polyamide: Alcohol	300:300:8:8:51
D1,D2,D3,D4	Sand: Barite: Epoxy resin: Polyamide: Alcohol	300:300:10:10:51

Table 2. Proportion of brittle material.

Number	Mixture	Mass ratio
E1,E2,E3,E4	Sand: Barite: Colophony: Alcohol	200:200:7:34
F1,F2,F3,F4	Sand: Barite: Colophony: Alcohol	200:200:9:34
G1,G2,G3,G4	Sand: Barite: Colophony: Alcohol	200:200:11:34
H1,H2,H3,H4	Sand: Barite: Colophony: Alcohol	200:200:13:34

The overall dimensions of specimens containing multiple flaws are 90 mm wide × 150 mm long × 70 mm thick. Flaws are created by inserting steel shims into nine slots in the mould template and removing them during curing. The steel shims are 20 mm wide x 1 mm thick, and the mould has interior dimensions of 150 mm × 90 mm × 70 mm, as shown in Fig. 2.

(a)   (b)

1. Download high-res image (146KB)
2. Download full-size image

Fig. 2. (a) The steel shims, which is used to create the flaws in the modelling material; (b) the mould, which is used to make the rock-like specimens.

In this paper, the artificially created fracture is described as flaw, while the newly propagating fracture is designated as crack. The geometry of the rock-like specimens containing multiple flaws is depicted in Fig. 3. The length of all pre-existing flaws is 2a = 20 mm, the flaw inclination angle is 60°. As shown in Fig. 3, nine flaws are placed in three rows with three flaws per row. The vertical distances between row and row are denoted as S_1 = 43 mm and S_2 = 38 mm, respectively. In addition, the horizontal distance between flaws in per row is denoted as d = 15 mm.
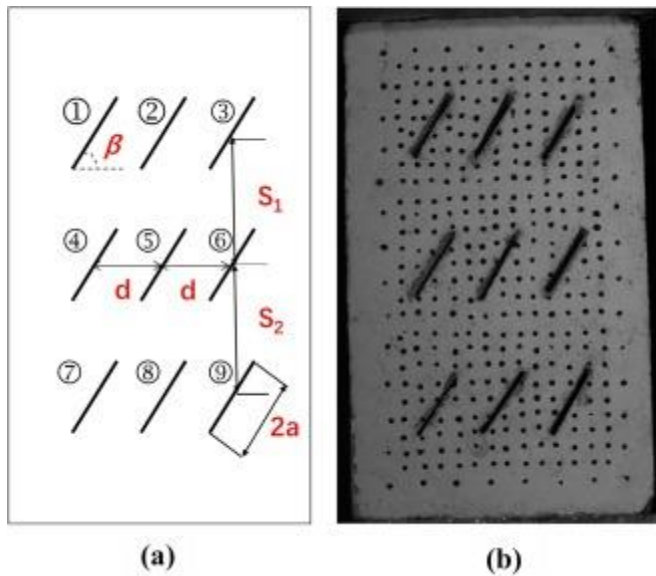
Fig. 3. Specimen containing multiple flaws with inclination angle $\beta = 60°$, length $2a = 20$ mm, horizontal distance between flaws $d = 15$ mm, vertical distances between flaws $S1 = 43$ mm, $S2 = 38$ mm.

In order to obtain reliable results when experiments are conducted, the specimen preparation process is implemented strictly and under well control. Attention has been paid to ensure that the mould is clean and dry, and lubricant is applied on the inner surface of the mould before the mixture paste is filled into the mould. Lubricant is also used to ensure that the steel shims' surface are smooth. Moreover, an oven set at a temperature of 20 °C is used to house the specimens for 18 h before the steel shims are pulled out of them. In the end, specimens are demolded and placed into a curing room for 21 days.

2.2. Testing system

In this paper, uniaxial compression tests are conducted by a RGM-611 computer controlelectronic universal testing machine, as shown in Fig. 4, under displacement-controlled conditions at an average loading rate of 1 mm/min. Therefore, it takes approximately 10–15 min until a specimens fails. Moreover, during the loading processes, the evolution processes of cracks in the rock-like specimens containing multiple flaws are captured by a XJTUDIC 3D full field deformation and strain measurement system. The measurement system includes two CCD video cameras, two LED illumination lamps and a computer, as shown in Fig. 5.

1. Download high-res image (180KB)
2. Download full-size image

Fig. 4. The uniaxial loading device: RGM-611 computer control electronic universal testing machine, Rieger instruments Ltd, in Shenzhen of China.

1. Download high-res image (101KB)
2. Download full-size image

Fig. 5. XJTUDIC 3D full field deformation and strain measurement system with two CCD video cameras, two LED illumination lamps.

First of all, two light-emitting diode (LED) lamps are switched on during the experiment to illuminate the rock-like specimens' surface, which enable two CCD video cameras, of which size in pixel reaches to 8 MP, to capture images of the rock surface. Secondly,

the images captured by cameras are transferred as digital signals and are sent to the computer. Finally, the images are used to interpret the surface deformation and strain fields by the program which was written based on the DSCM in the computer. More details about the principle or basic idea of how DSCM further analyzes the deformation and strain filed around the pre-existing crack surfaces have been extensively studied by some researchers [32], [33]. DSCM has become a normally accepted technique to investigate displacement and strain in rock experiments. During the experiment process, in order to capture the fracturing process on the rock surface accurately and effectively, the capture rate in frames per second changes as follows: one frame/s before noticeable crack propagation occurs in specimens; 5 frames/s during the initiation phase of crack propagation; 15 frames/s in the period of more intensive cracking phase.

2.3. Digital image correlation (DIC)

DIC is an optical method that deals with a reference image recorded before deformation and a series of deformed images recorded after deformation. The basic principle of DIC is to track the same pixel points located in various deformed images [34], as shown in Fig. 1. Normally, a square subset or the so called subimage centered at the considered point, rather than a single pixel, is tracked in the deformed images using selected correlation function such as zero-normalized cross-correlation (ZNCC) [34]. By minimizing or maximizing the correlation coefficient [35], the location of a square subset in the deformed image is found and the displacement components of this subset center can be determined. The corresponding point P′(x′,y′) after deformation related to the coordinate P(x,y) in reference image can be calculated as:

$$(1) \quad x' = x + u + \frac{\partial u}{\partial x}\Delta x + \frac{\partial u}{\partial y}\Delta y \quad y' = y + v + \frac{\partial v}{\partial x}\Delta x + \frac{\partial v}{\partial y}\Delta y$$

where u and v are respectively the displacement components of the subset center point O in x, y directions, Δx and Δy are respectively the distances from point P to point O in x, y directions, $\frac{\partial u}{\partial x}$, $\frac{\partial u}{\partial y}$, $\frac{\partial v}{\partial x}$ and $\frac{\partial v}{\partial y}$ are the gradients of displacement components for the subset shown in Fig. 6.
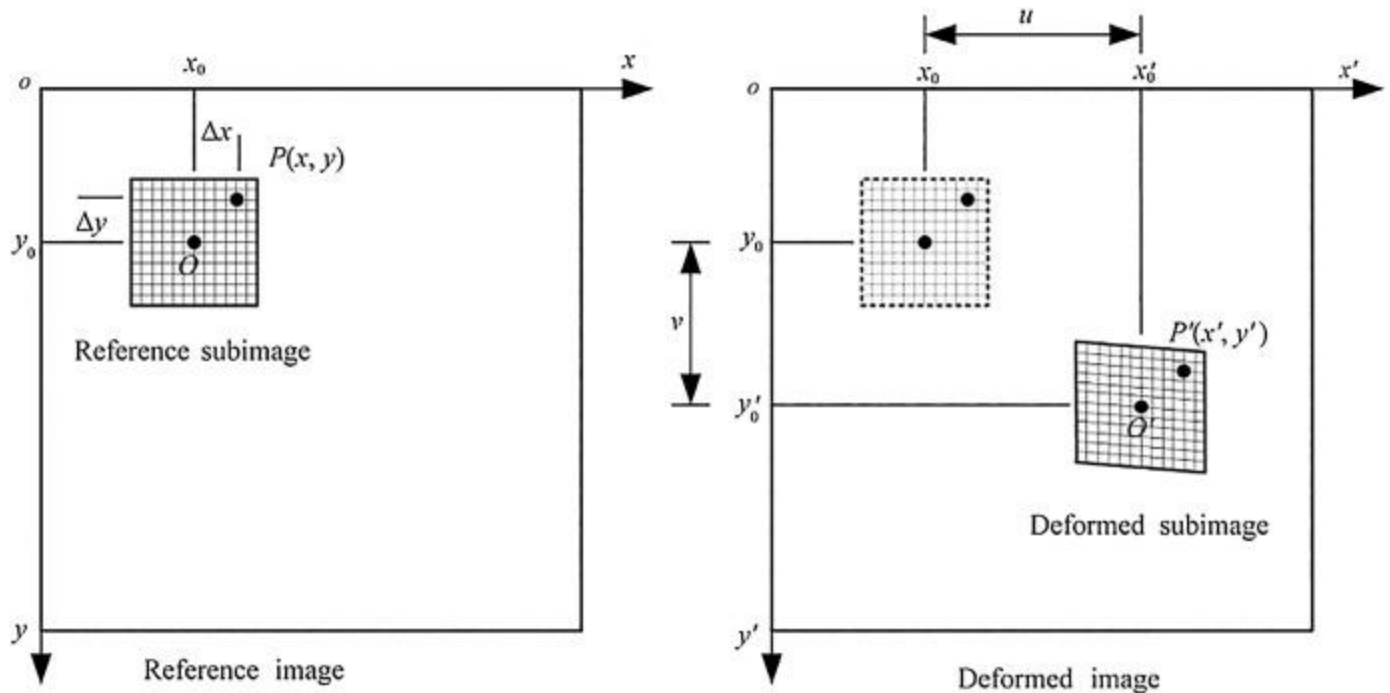
Fig. 6. Schematics of reference and deformed subsets [35].

The horizontal displacement u and the vertical displacement v can be determined when the corresponding point P'(x',y') after deformation related to the coordinate P(x,y) in reference image is successfully searched. If the same tracking procedure is repeated on the other points on the surface of specimens, full-field displacements of the zone of interest (ZOI) are obtained [34]. Finally, the full-field strains can be spontaneously determined from the full-field displacement.

2.4. Calibration of DSCM

To illustrate the veracity of the DSCM, a shear test was conducted on a homogeneous PMMA specimen, of which overall dimensions are 190 mm wide × 200 mm long × 10 mm thick. The specimen contains a 100-mm-long pre-existing flaw and strain gauges with grating area of 3 mm × 5 mm are glued on the surface of PMMA specimen to obtain strains information during shear loading, as shown in Fig. 7(a). The contour of horizontal strain calculated by DSCM software is also shown in Fig. 7(b). From Fig. 7(b), strain concentration occurs near the pre-existing flaw. The shorter distance from the center of the pre-existing flaw, the larger the strain is. To demonstrate the accuracy of strain value by DSCM, three zones that are adjacent to the three stain gauges, as marked by red square in Fig. 7(a), are selected as "DSCM zones". Average strain of each of

these three zones calculated by DSCM is compared with that directly obtained value by strain gauges, the result is presented in Fig. 8. The calculated horizontal strain is in good agreement with the measured horizontal strain. Moreover, strain value measured by strain gauge 3, whose distance is closer to the center of the pre-existing flaw, is bigger than those measured by gauge 1 and 2. It is found from Figs. 7(b) and 8(8) that the calculated characters of horizontal strain are in good agreement with the measured characters of horizontal strain. Thus, it can be concluded that strain can be captured accurately by DSCM, and this calibration provides both the veracity and the reproducibility of the strain analysis.
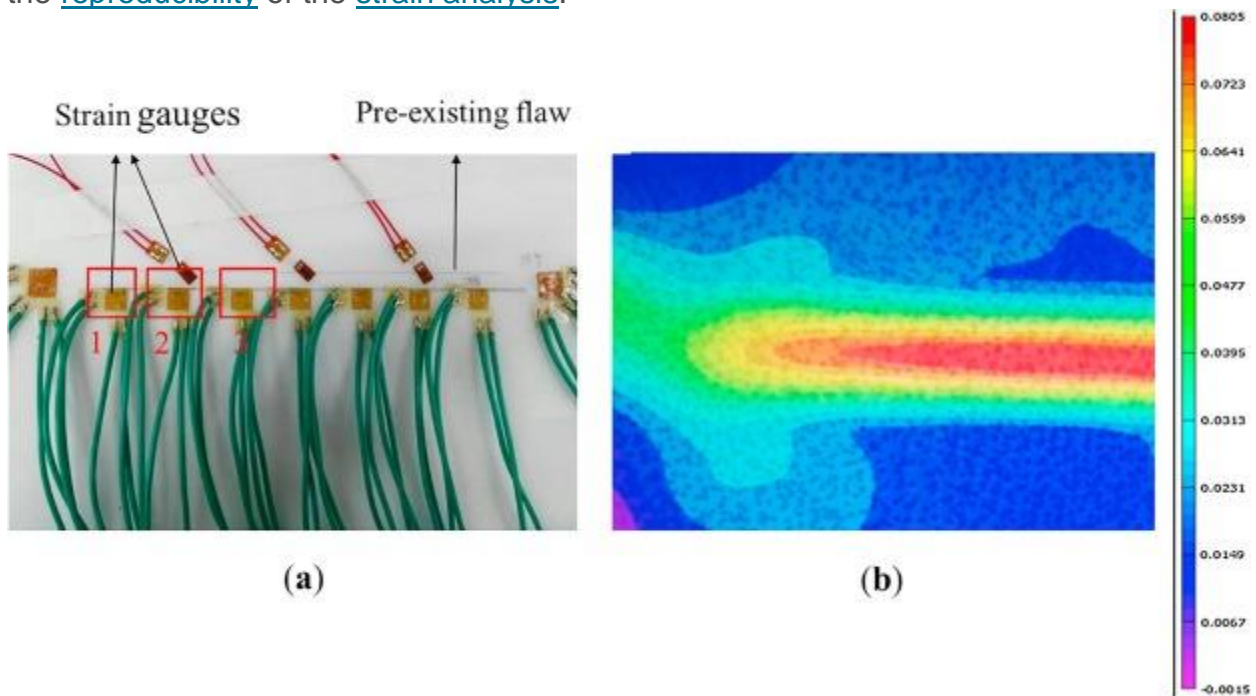
1. Download high-res image (293KB)
2. Download full-size image
   Fig. 7. (a) PMMA specimen containing a pre-existing flaw and glued with strain gauges; (b) contour of horizontal strain of the specimen under shearing loading.
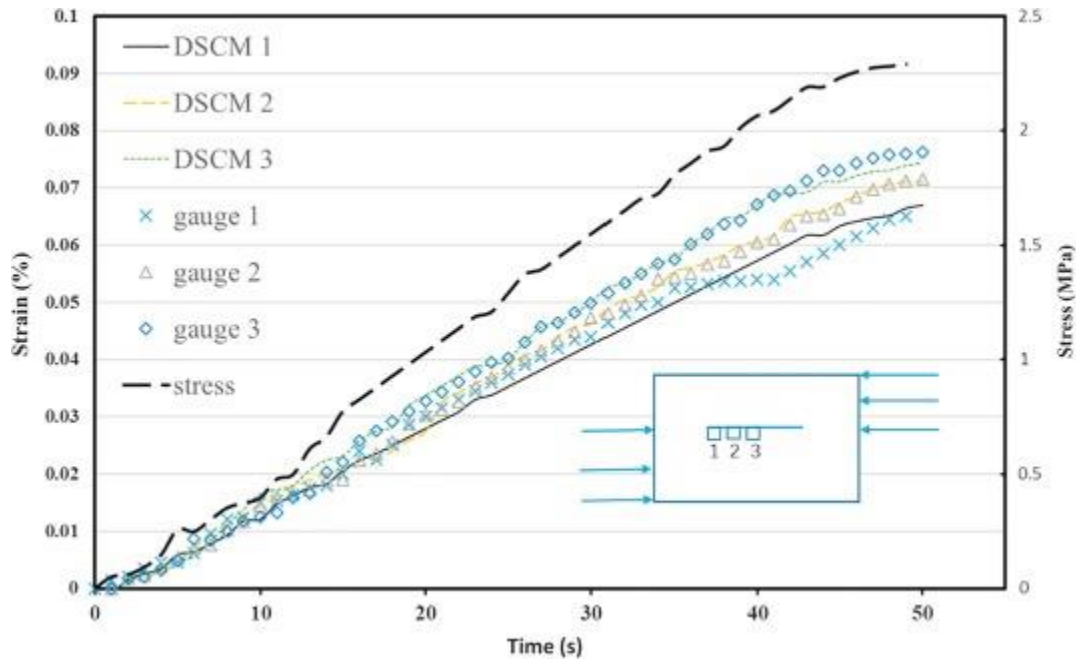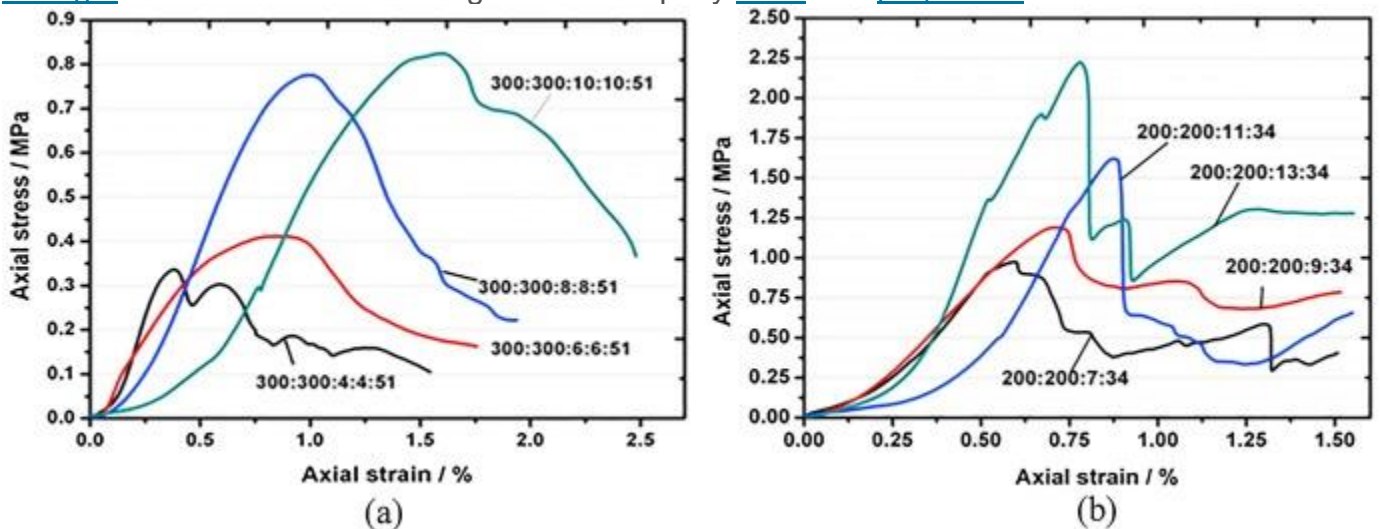
Fig. 8. Calibration of digital speckle correlation method (DSCM).

3. Experimental results

3.1. Axial stress-strain behavior

Fig. 9(a) illustrates the axial stress-strain curves of ductile rock-like specimens containing multiple flaws under uniaxial compression. Fig. 9(a) shows that the axial stress-strain curves represent the deformation characters of ductile rocks under uniaxial compression, in which the strain softening occurs in the post-peak region, and the peak strength increases with increasing content of epoxy resin and polyamide.

Fig. 9. Effect of mass ratio on axial stress-strain curves of specimens: (a) ductile specimens, mixture of Sand: Barite: Epoxy resin: Polyamide: Alcohol; (b) brittle specimens, mixture of Sand: Barite: Colophony: Alcohol.

Fig. 9(b) shows the axial stress-strain curves of brittle rock-like specimens under uniaxial compression. Fig. 9(b) shows that the axial stress-strain curves represent the deformation characters of brittle rock-like material under uniaxial compression, in which rapid stress drop occurs in the post-peak region, and the peak strength increases with increasing content of colophony.

All the curves of stress-strain of ductile and brittle material specimens share a common ground in the pre-peak regime, which can be sub-divided into three stages, namely initial compaction stage, linear elastic stage and nonlinear elastic stage. However, a distinct difference can be observed in the stress-strain curves in the post-peak regime. For the ductile materials, strain softening occurs in the post-peak regime, whereas for the brittle materials, rapid stress drop occurs in the post-peak regime.

Fig. 10 shows the effect of mass ratio on the average peak strength of rock-like materials containing multiple flaws under uniaxial compression. It also reveals that the average peak strength of ductile rock-like materials increases from 0.291 MPa to 0.909 MPa with increasing contents of epoxy resin and polyamide, whereas the average peak strength of brittle rock-like material specimens increases from 1.093 MPa to 2.318 MPa with increasing content of colophony. It should be noted that the average peak strength of brittle materials are higher than that of ductile materials.
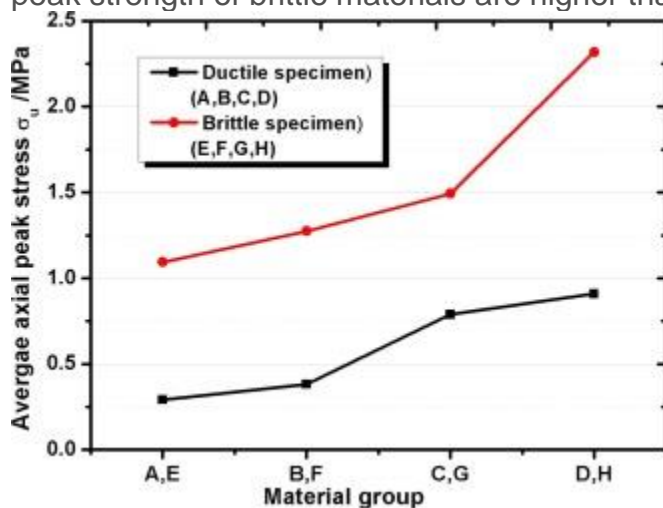
Fig. 10. Effect of mass ratio on the average peak strength of rock-like materials containing multi flaws under uniaxial compression.

In this paper, the brittleness index proposed by Meng et al. [36] is adopted, which can be expressed as follows:

$$(2) \quad B_d = B_{1d} B_{2d} = \frac{\tau_p - \tau_r}{\tau_p} \cdot \log|k_{ac}|_{10}$$

where τ_p is the peak strength and τ_r is the residual strength in the complete stress-strain curve of the intact rock-like specimen, B_{1d} describes the relative post-peak stress drop, which varies from 0 to 1, B_{2d} denotes the velocity of the post-peak stress decrease and k_{ac} represents that the slope of the line segment from the initial yielding point to the starting point of the residual strength.

Eq. (2) indicates that the peak stress is equal to the residual stress when $B_{1d} = 0$. However, $B_{1d} = 1$ means that the residual stress is null. The larger values of B_{1d} and B_{2d} allow for the larger value of B_d, and the larger value of B_d indicates the higher brittleness of rock-like materials.

The stress drop velocity can be calculated by the following formulation:

$$(3) \quad k_{ac} = \frac{\tau_a - \tau_c}{\varepsilon_a - \varepsilon_c}$$

in which ε_a and τ_a are, respectively, the axial strain and stress at the initial yielding point, ε_c and τ_c are the axial strain and stress at the starting point of the residual strength, respectively.

The average B_d – values of ductile and brittle specimens are shown in Table 3, Table 4, respectively. It can be found from Table 3 that the brittleness index of ductile material decrease with increasing contents of epoxy resin and polyamide, that is, ductility increases when more epoxy resin and polyamide are used. However, brittleness index of brittle material increases with increasing content of colophony, as shown in Table 4.

Table 3. Brittleness index of ductile material.

Group	Mass ratio (Sand: Barite: Epoxy resin: Polyamide: Alcohol)	Brittleness index (Bd)
A	300:300:4:4:51	10.85%
B	300:300:6:6:51	9.12%
C	300:300:8:8:51	6.77%
D	300:300:10:10:51	6.49%

Table 4. Brittleness index of brittle material.

| Group	Mass ratio (Sand: Barite: Colophony: Alcohol)	Brittleness index (Bd)
E	200:200:7:34	10.31%

Group	Mass ratio (Sand: Barite: Colophony: Alcohol)	Brittleness index (Bd)
F	200:200:9:34	12.22%
G	200:200:11:34	13.45%
H	200:200:13:34	15.88%

3.2. Crack behavior in the specimens

In order to investigate the effect of brittleness on the crack behavior, fracture process of three specimens, of which value of brittleness index respectively equals to 6.49%, 10.85% and 15.88%, are discussed below.

3.2.1. Fracturing process of multi-flawed specimens

In this paper, "T" represents wing crack, "AT" denotes anti-wing crack, "CS" suggests coplanar secondary crack, and "OS" means oblique secondary crack, "FC" indicates far field crack. Tips of pre-existing flaws are named as follows: the left tip of a single pre-existing flaw is named as tip a and the right tip is named as tip b, as shown in Fig. 11(b). Therefore, T9a represents wing crack initiating from tip a of pre-existing flaw ⑨, CS7a and OS8a respectively represents coplanar secondary crack initiating from tip a of pre-existing flaw ⑦ and oblique secondary crack initiating from the tip a of pre-existing flaw ⑧, as shown in Fig. 11(b). In addition, CS7bCS5a represents the coalescence of coplanar secondary crack initiating from the tip b of pre-existing flaw ⑦ and coplanar secondary crack initiating from the tip a of pre-existing flaw ⑤, as shown in Fig. 11(b).

(a)   (b)
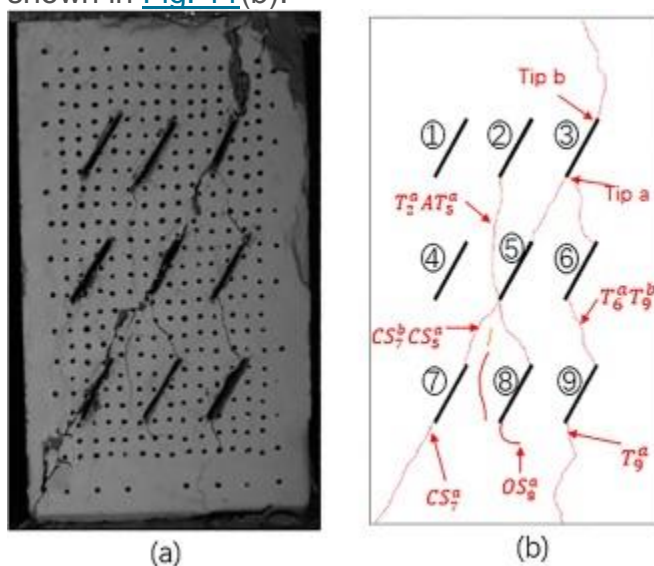
1. Download high-res image (159KB)
2. Download full-size image

Fig. 11. Convention of cracking behavior in the specimen.

3.2.1.1. Ductile specimens

For ductile material specimens, D3 and A1, are taken as typical examples for fracture process investigation.
Fig. 12 shows crack initiation, growth and coalescence process in specimen D3 containing nine pre-existing flaws under uniaxial compression as well as the corresponding vertical strain fields captured by the DIC technique. The stress-strain curve is plotted in Fig. 13.

(a)0.866σ_{peak} (b)0.921σ_{peak}

(c)0.994σ_{peak} (d)1.000σ_{peak}

(e)0.753σ_{peak} (f)0.438σ_{peak}
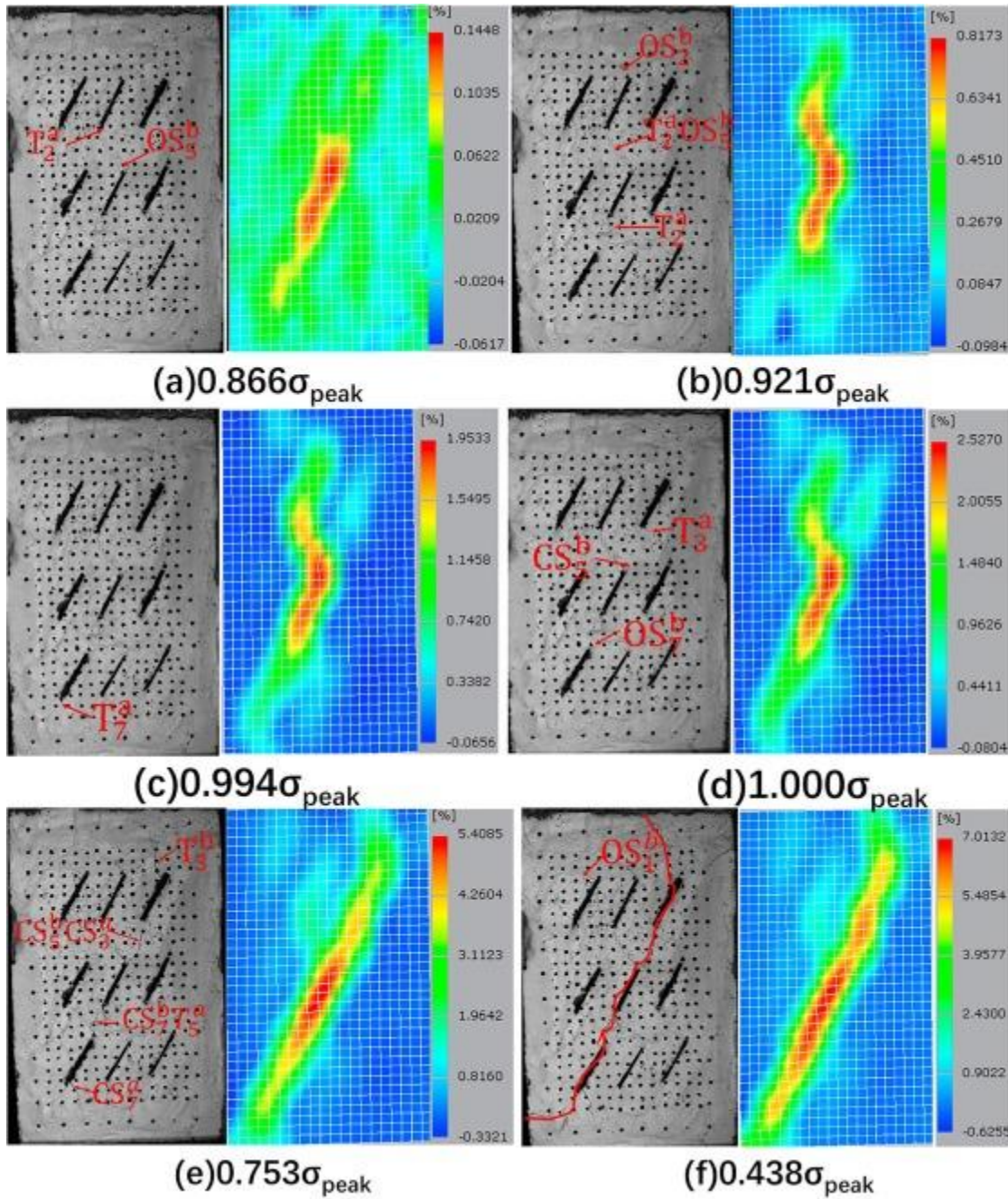
1. Download high-res image (1MB)
2. Download full-size image

Fig. 12. Cracking process and the contour of the vertical strain fields in ductile specimen D3 (brittleness index: 6.49%) containing multiple flaws under uniaxial compression.
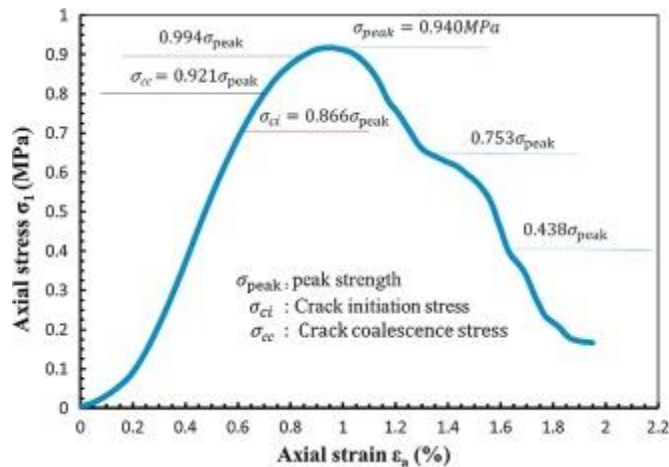
Fig. 13. Axial stress-strain curve of specimen D3 under uniaxial compression.

When specimen D3 is loaded to 0.866 σpeak, oblique secondary crack OS5b and wing crack T2a simultaneously and respectively initiate from tip b of flaw ⑤and tip an of flaw ②, the strain concentrates around the flaw ⑤, the maximum value of the vertical strain is equal to 0.145%, as shown in Fig. 12(a). When the stress increases to 0.921σpeak, coalescence of oblique secondary crack OS5b and wing crack T2a occurs. Meanwhile, oblique secondary crack OS2binitiates from tip b of flaw ②, wing crack T5a initiates from tip a of flaw ⑤, and strain localization is induced by the coalescencing crack OS5bT2a, in which the maximum value of strain is 0.817%, as shown in Fig. 12(b). When the stress reaches 0.994σpeak, wing crack T7a initiates from tip a of flaw ⑦, the width of the coalescencing crack OS5bT2a increases, and the maximum value of strain increases to 1.953%, as shown in Fig. 12(c). When the specimen is loaded to peak strength of 0.940 MPa, coplanar secondary cracks CS5b and CS7brespectively initiate from tip b of flaw ⑤and ⑦, and wing crack T3a initiates from tip a of flaw ③, as shown in Fig. 12(d). Beyond the peak stress, new coplanar secondary crack CS3ainitiating from tip a of flaw ③coalesces with coplanar secondary crack CS5b, and crack coalescence can also be observed between coplanar secondary crack CS7b and wing crack T5a, macrocrack preliminarily forms from these crack coalescence behavior, and strain localization band occurs around the macrocrack, leading to a stress drop in the curve of stress-strain from the peak strength to 0.753 σpeak, where the maximum strain value reaches 5.409%, as shown in Fig. 12(e). When the applied stress drops to 0.438σpeak, the macrocrack propagates to the top and bottom boundaries of the specimen, leading to a pure-shear failure mode of the specimen, as shown in Fig. 12(f).

Fig. 14 shows crack initiation, growth and coalescence process in specimen A1 containing nine pre-existing flaws under uniaxial compression as well as the corresponding vertical strain fields captured by the DIC technique. The stress-strain curve of specimen A1 is plotted in Fig. 15.

(a) $0.952\sigma_{peak}$

(b) 0.964_{peak}

(c) $0.772\sigma_{peak}$

(d) $0.522\sigma_{peak}$

(e) $0.470\sigma_{peak}$

(f) $0.313\sigma_{peak}$
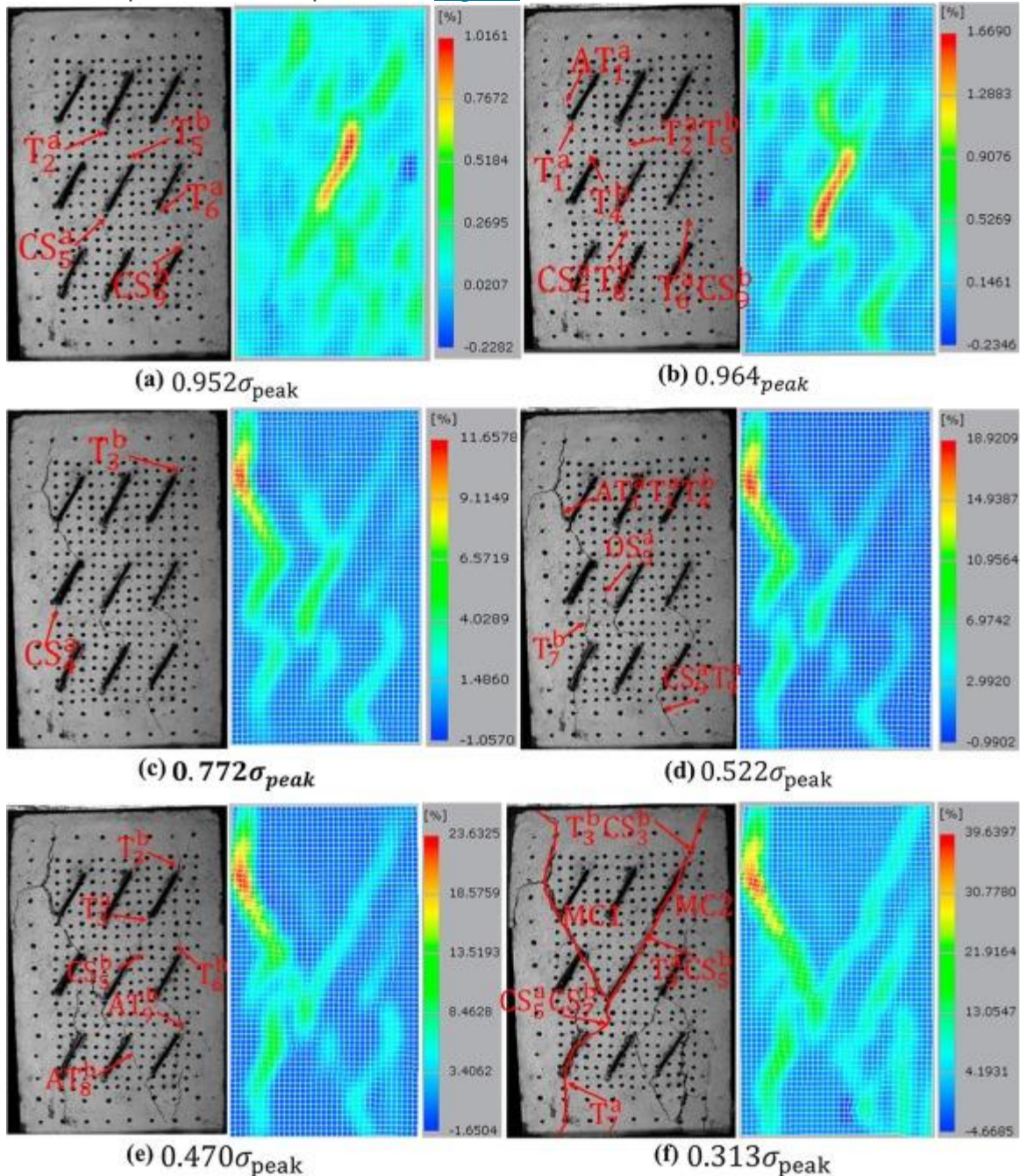
1. Download high-res image (2MB)
2. Download full-size image

Fig. 14. Cracking process and the contour of the vertical strain fields in ductile specimen A1 (brittleness index: 10.85%) containing multiple flaws under uniaxial compression.
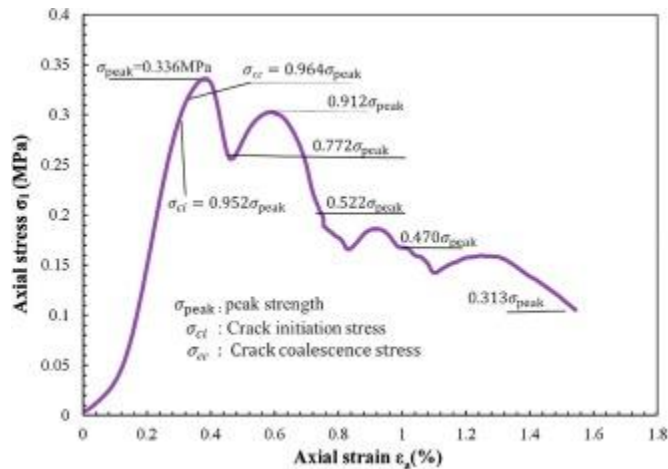
1. Download high-res image (119KB)
2. Download full-size image

Fig. 15. Axial stress-strain curve of specimen A1 under uniaxial compression.

When specimen A1 is loaded to 0.952 σpeak, strain concentrates around tips of pre-existing flaws ②, ⑤, ⑥ and ⑨, the maximum value of vertical strain is 1.016%, which is located near the tip b of flaw⑤, as shown in the contour of vertical strain fields in Fig. 14(a). Meanwhile, three wing cracks, T2a,T5b, T6a, and two coplanar secondary cracks, CS5a and CS9b, firstly and almost synchronously initiate from tips of pre-existing flaws ②, ⑤, ⑥ and ⑨, as shown in Fig. 14(a). The reason for simultaneous initiation of cracks is that the specimen contains multiple pre-existing flaws and the flaw spacing is small enough to cause crack initiation at the same time. When the specimen is loaded to 0.964σpeak, wing crack T2a initiating from tip a of flaw② coalesces with wing crack T5b initiating from tip b of flaw ⑤, wing crack T6a initiating from the tip a of flaw ⑥coalesces with coplanar secondary crack CS9b initiating from tip b of flaw ⑨, wing crack T8b initiating from tip b of flaw ⑧coalesces with coplanar secondary crack CS5ainitiating from tip an of flaw⑤, leading to the strain localization and crack coalescence between flaws ②and ⑤, flaws ⑥and ⑨, flaws ⑧and ⑤, as shown in Fig. 14(b). At the same time, anti-wing crack AT1a and wing crack T1a initiate from tip a of pre-existing flaw ①, and propagate along the loading direction, the strain concentrates in the tip of the pre-existing flaw ①, and the vertical strain increases to 1.669%. When specimen A1 is loaded to 0.336 MPa, specimen A1 reaches the maximum bearing capacity. After that, the bearing capacity of specimen A1 decreases. When the stress drops to 0.772σpeak, wing cracks T3b and coplanar secondary crack CS4arespectively initiate from tip b of flaws ③and ④, as shown in Fig. 14(c). Meanwhile, wing crack T1a initiating from tip a of flaw ①coalesces with wing crack T4b initiating from tip b of flaw ④, leading to the first sudden stress drop in the

curve of axial stress-strain, as shown in Fig. 14. It should be noted that, from Fig. 14(c), the width of the first macrocrack (MC1) induced by the coalescence of wing cracks T1a and T4b increases. An interesting phenomenon can also be found from the vertical strain field in Fig. 14(c) that strain localization occurs near the first macrocrack (MC1), in which the maximum strain reaches to 11.658%. After that, the bearing capacity of specimen A1 increases to $0.914\sigma_{peak}$, the width of the first macrocrack (MC1) continues to increase and the corresponding maximum strain also increases to 18.921%. Meanwhile, oblique secondary crack OS5a and wing crack T7b respectively emanate from the tip an of flaw ⑤ and the tip b of flaw ⑦, leading to the second stress drop from $0.912\sigma_{peak}$ to $0.522 \sigma_{peak}$ in the stress-strain curve, as shown in Fig. 15. When the stress drops to $0.470\sigma_{peak}$, as shown in Fig. 14(e), wing crack T3b initiating from tip b of flaw ③ coalesces with coplanar secondary crack CS3b initiating from tip b of flaw ③, coplanar secondary crack CS5a initiating from tip a of flaw ⑤ coalesces with wing crack T3a initiating from tip a of flaw ③, coplanar secondary crack CS5a initiating from the tip a of flaw ⑤ links with coplanar secondary crack initiating from the tip b of flaw ⑦, leading to the formation of the second macrocrack (MC2). Due to these two macrocracks mentioned above, the specimen fails in X-like shaped mode. The failure mode of the ductile material specimen is mainly dominated by the coplanar secondary cracks. It should be noted that the first coalescencing crack T2aT5b occurring at $0.964 \sigma_{peak}$ is close and stops propagating when the stress drops to $0.522\sigma_{peak}$, as shown in Fig. 14(d).

In addition, Fig. 14 shows that cracking behavior captured by DIC technique are consistent with those captured by the CCD cameras, and DIC technique is reliable to track the crack initiation, propagation and coalescence behavior.
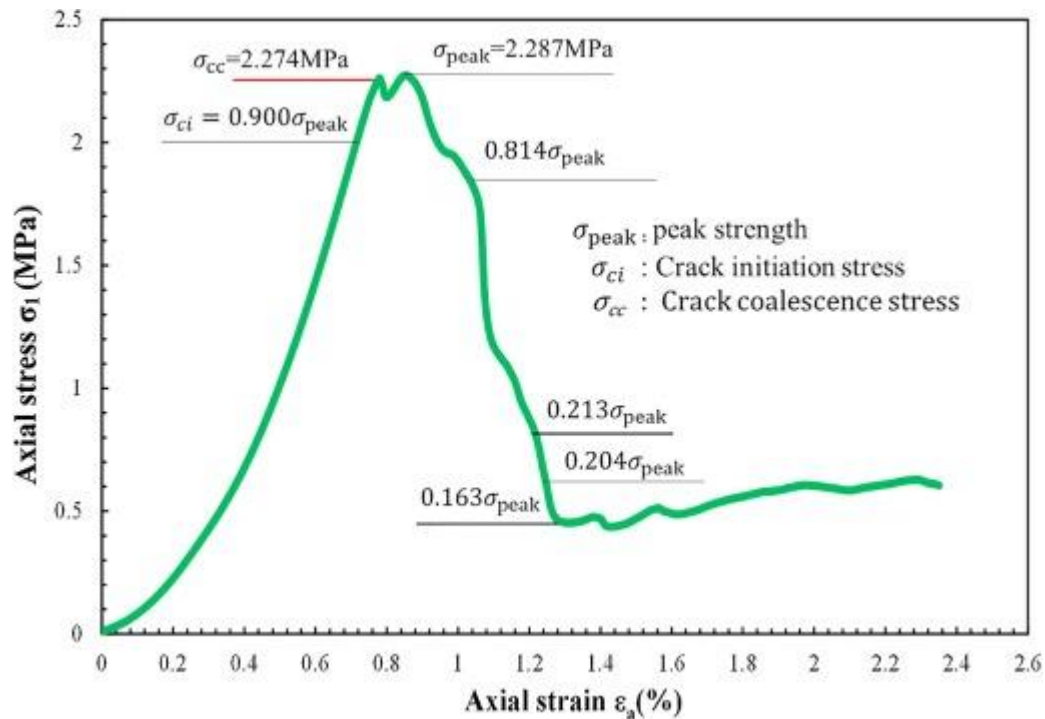
3.2.1.2. Brittle specimens

In this subsection, a representative specimen H1 with brittleness index of 15.88% is selected to analyze the fracturing process in brittle materials. Fig. 16 shows fracturing process and the corresponding vertical strain field in brittle specimen H1. Fig. 17 presents the complete stress-strain curve of specimen H1.

(a) $0.900\sigma_{peak}$

(b) $1.000\sigma_{peak}$

(c) $0.814\sigma_{peak}$

(d) $0.213\sigma_{peak}$

(e) $0.204\sigma_{peak}$

$0.163\sigma_{peak}$
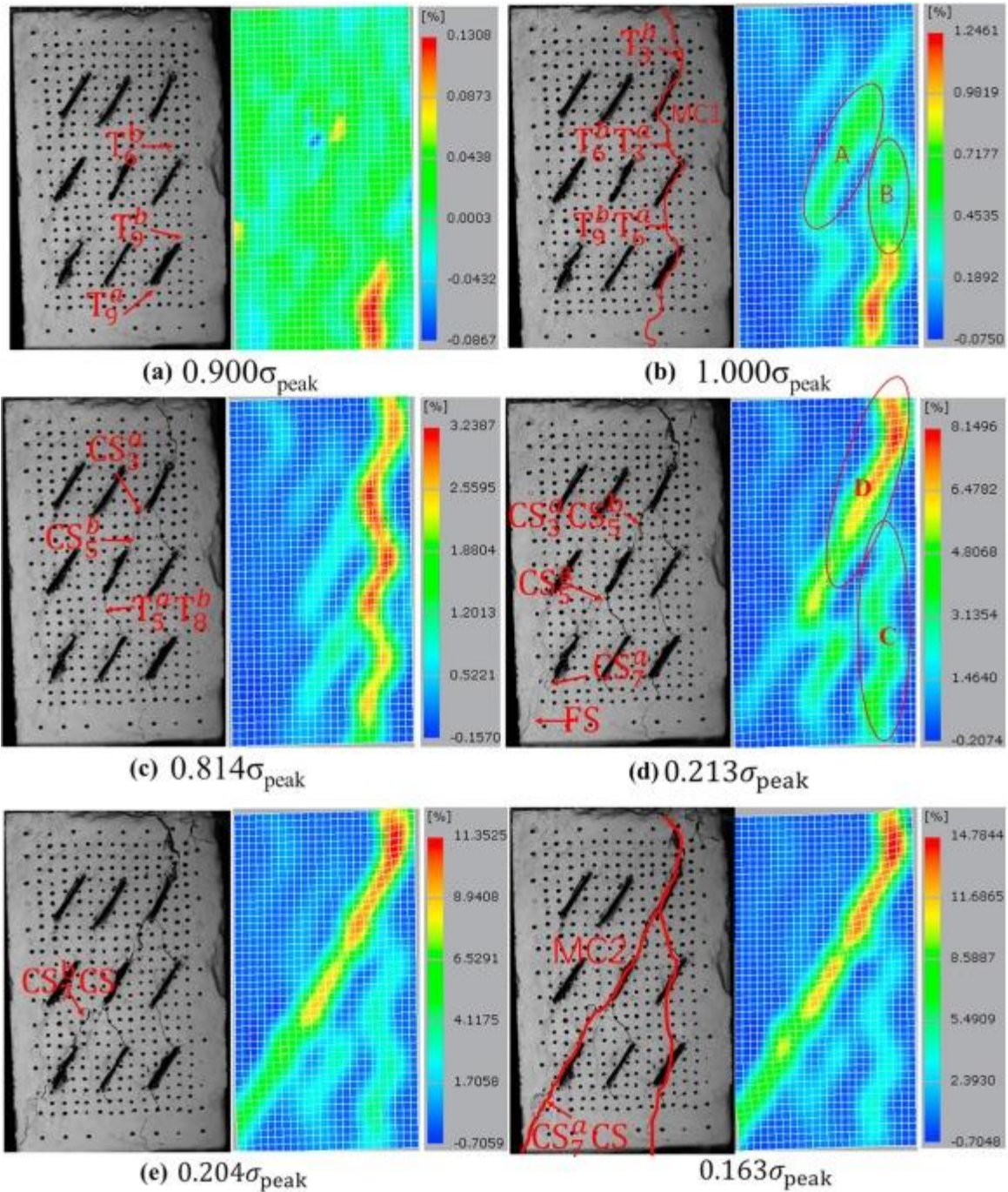
1. Download high-res image (2MB)
2. Download full-size image

Fig. 16. Cracking process and the contour of the vertical strain fields in brittle specimen H1 (brittleness index: 15.88%) containing multiple flaws under uniaxial compression.

Fig. 17. Axial stress-strain curve of brittle specimen H1 under uniaxial compression.

When specimen H1 is loaded to 0.900σpeak, wing cracks T6b and T9b respectively initiate from tip b of flaw ⑥and tip b of flaw ⑨, and propagate along the upward direction of the specimen, wing crack T9a initiates from tip a of flaw⑨ and propagates along the downward direction of the specimen H1, as shown in Fig. 16(a).
When the stress increases to 0.994σpeak, wing cracks T3b and T9a respectively initiate from tip b of flaw ③and tip a of flaw ⑨, wing crack T6a initiates from tip a of flaw ⑥ and quickly links with wing crack T9b, leading a minor stress drop in the curve of the stress-strain, as shown in Fig. 17. When the specimen is loaded to peak strength 2.287 MPa, a wing crack T3a initiates from tip a of flaw ③ and coalesces with wing crack T6b initiating from tip b of flaw ⑥. Meanwhile, T3b and T9a respectively reach the top and bottom boundary of the specimen, leading to the formation of the first macrocrack (MC1) and strain localization occurs near the first macrocrack (MC1), as shown in Fig. 16(b). Beyond the peak strength, formation and propagation of this first macrocrack (MC1) lead to the splitting failure in the specimen and the rapid drop in the curve of stress-strain, as shown in Fig. 17.
When the applied stress drops to 0.814σpeak three coplanar secondary cracks CS5a, CS5b and CS3a simultaneously and respectively initiate from tips of flaw

⑤ and tip an of flaw③, and wing crack T5a initiating from tip a of flaw ⑤ coalesces with wing crack T8b initiating from tip b of flaw ⑧, as shown in Fig. 16(c).

When the applied stress drops to 0.213σpeak, coalescence of two coplanar secondary cracks CS5b and CS3a leads to the occurrence of strain localization band marked as SL, and the maximum value of the corresponding strain reaches to 8.150%, as shown in Fig. 16(d). Meanwhile, two coplanar secondary cracks CS7a and CS7b simultaneously initiate from tips of flaw ⑦, and the far field crack FC initiates near the left side of specimen H1.

When the applied stress drops to 0.204σpeak, coalescence of coplanar secondary cracks CS3a,CS5a,CS5b,CS7a,CS7b and wing crack T3b leads to the formation of the second macrocrack (MC2) and the failure of specimen H1, and stress drops to the residual stress level, as shown in Fig. 17(f).

By comparing fracturing process and failure mode of specimen D3, A1 and H1 containing multiple flaws, the difference can be summarized as follows:

(1)

Crack initiation mode: Compared with specimen D3, five cracks including three wing cracks and two coplanar secondary cracks, initiate firstly and synchronously in specimen A1; whereas, three wing cracks initiate firstly in specimen H1. Thus, it can be concluded that tensile crack easily occurs as the brittleness index of the specimen increases, as shown in Table 5.

Table 5. A comparison of the experimental initiation stress, initiation mode and failure mode.

Specimen	Brittleness index	Ratio of initiation stress to the peak strength	Initiation mode	Failure mode
D3	6.49%	0.866σpeak	T2a,OS5b	Pure shear
A1	10.85%	0.952σpeak	T2a,T5b,T6a,CS5a,CS9b	Tension-shear
H1	15.88%	0.900σpeak	T9a, T6b,T9b	Tensile

(2)

Failure mode: Table 5 shows that the pure shear failure mode occurs in ductile specimen D3, the mixed shear-tension failure mode occurs in the specimen A1, and the splitting failure mode occurs in brittle specimen H1. That is to say, the failure mode of specimens transforms from the pure shear failure to the mixed tension-shear, then to the splitting failure as the brittleness index increases. Fig. 18 shows the fracturing behavior of brittle specimens F4, G1, G2 and H2 with the

brittleness index of 12.22%, 13.45%, 13.45% and 15.88%. It can be found from Fig. 18 that the coalescence of wing cracks easily occurs in brittle specimens, leading to the splitting failure. It is quite different from ductile specimens with a low brittleness index, of which failure mode is dominated by the coalescence of coplanar secondary cracks.
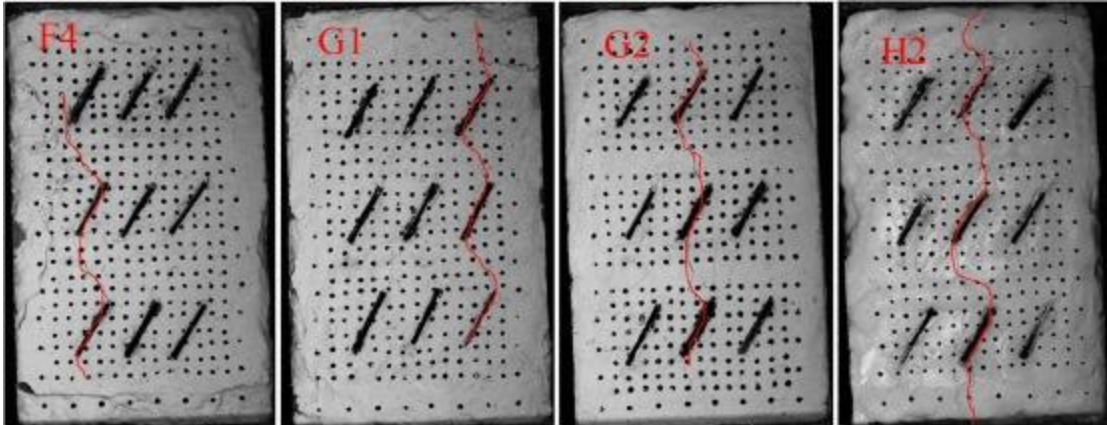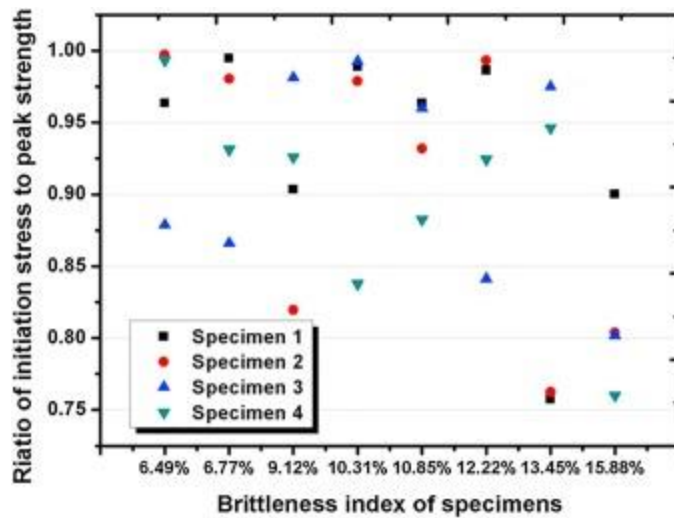

1. Download high-res image (408KB)
2. Download full-size image

Fig. 18. The wing crack coalescence in brittle specimens.

4. Crack initiation, coalescence and failure mode

4.1. Initiation stress

In order to understand the effect of brittleness on the fracture mechanism of ductile and brittle rocks, the first crack initiation stress is defined as the initiation stress and the ratio of initiation stress to peak strength of all the specimens are plotted in Fig. 19. Fig. 19(a) shows the ratio of initiation stress to peak strength in all the specimens with various brittleness index and Fig. 19(b) presents the average ratio of initiation stress.
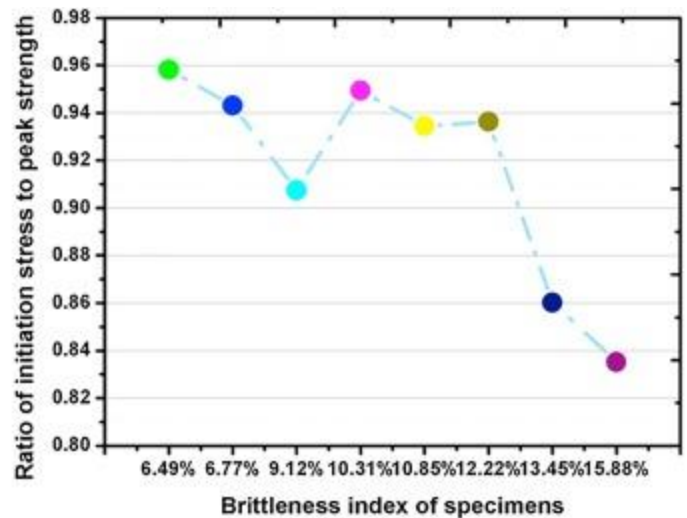
Fig. 19. Initiation stress in specimens with various brittleness index: (a) distribution of ratio of initiation stress to the peak strength; (b) the average ratio of initiation stress to the peak strength.

Fig. 19(a) reveals that for the ductile specimens, the ratio of initiation stress to the peak strength varies from 0.8 to 1.00; while for the brittle specimens, the ratio of initiation stress to the peak strength changes from 0.75 to 1.00. In general, the average ratio of initiation stress to the peak strength in brittle specimens is lower than that in ductile specimens, as shown in Fig. 19(b).

Fig. 19(b) also shows that for the ductile specimens, the ratio of initiation stress to the peak stress tends to decrease with increasing brittleness index when the brittleness index is approximately lower than 10%, while for brittle specimens, the ratio of initiation stress to the peak strength tends to decrease with an increase in the brittleness index when the brittleness index is approximately more than 10%.

4.2. Initiation modes

To investigate the effect of the brittleness index on crack initiation modes in ductile and brittle specimens containing multiple pre-existing flaws, crack initiation modes are summarized in Table 6.

Table 6. The first initiated cracks in ductile and brittle specimens.

Ductile specimens	Brittleness index	The first initiated crack	Brittle specimens	Brittleness index	The first initiated crack
A1	10.85%	T2a,T5b,T6a,CS5a,CS9b	E1	10.31%	T4a,T7b,OS1b

Ductile specimens	Brittleness index	The first initiated crack	Brittle specimens	Brittleness index	The first initiated crack
A2		OS3a,OS2b,T3a	E2		T5a,T7b
A3		CS3b,CS3a	E3		T3a,T5a,CS5a
A4		T3a,OS3a,OS2b	E4		CS5b,T5a
B1	9.12%	CS8b,CS6a,T3b,T6b	F1	12.22%	T4a,T1a
B2		CS7b,CS5a,T3a	F2		AT1a,OS1b,AT3a
B3		CS5a,T3a	F3		CS7b,OS2a,CS5a
B4		CS5a	F4		T4b,T7b
C1	6.77%	CS3a	G1	13.45%	T6b,T9b,T3b,T6b
C2		CS4a,T7b	G2		T2b,T5a
C3		CS5a	G3		T4b,T7a
C4		OS1a,OS3a	G4		T4a,T1a,T7b
D1	6.49%	CS5b	H1	15.88%	T6b,T9a,T9b
D2		CS3a	H2		T2a,T5bT5a,T8b,T8a
D3		CS2a	H3		T5a,T5b,CS3a
D4		FC	H4		T4b,AT5a

For the ductile specimens, four crack initiation modes are observed, including wing crack (T), coplanar secondary crack (CS), oblique secondary crack (OS) and far field crack (FC), as shown in Table 6. For the brittle specimens, four crack initiation modes are also observed, which include wing crack (T), coplanar secondary crack (CS), oblique secondary crack (OS) and anti-wing crack (AT).

In general, the number of the first initiated cracks increases with an increase in the brittleness index for both ductile and brittle specimens. For the ductile specimens, when the value of brittleness index equals 6.49%, there is no tensile crack (wing crack or anti-wing crack) observed in the specimen, where only coplanar secondary crack and far field crack occur; while wing crack may initiate together with coplanar secondary crack or oblique secondary crack firstly and simultaneously when the value of brittleness index varies from 6.77% to 10.85%, as shown in Table 6. Therefore, in the ductile specimens, the crack initiation mode is mainly dominated by shear crack (coplanar secondary crack or oblique secondary crack). For the brittle specimens, the initiation mode is mainly dominated by tensile crack (wing crack or anti-wing crack), as shown in Table 6.
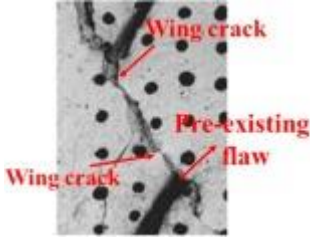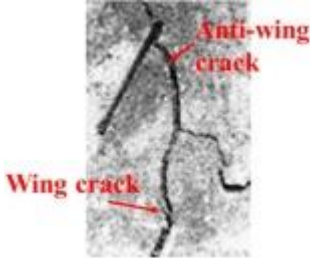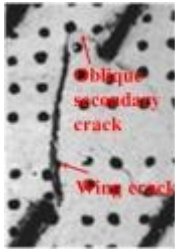
4.3. Coalescence modes

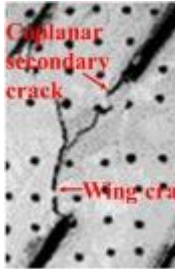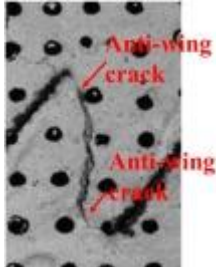The coalescence types observed in the ductile and brittle specimens are listed in Table 7. In Table 7, CST-2 represents two coalescencing cracks formed from the coalescence of coplanar secondary crack and wing crack. OSOS-2 represents two coalescencing cracks formed from the coalescence of two oblique secondary cracks. It can be found from Table 7 that nine coalescence types, including coalescence of two wing cracks (TT), coalescence of wing crack and anti-wing crack (ATT), coalescence of wing crack and oblique secondary crack (OST), coalescence of wing crack and coplanar secondary crack (CST), Coalescence of two anti-wing cracks (ATAT), coalescence of anti-wing crack and coplanar secondary crack (CSAT), coalescence of two oblique secondary cracks (OSOS), coalescence of coplanar secondary crack and oblique secondary crack (CSOS), coalescence of two coplanar secondary cracks (CSCS), are observed in ductile specimens, while except coalescence of coplanar secondary crack and oblique secondary crack (CSOS), other eight coalescence types occur in brittle specimens. All coalescence types found in ductile and brittle specimens are shown in Table 8.

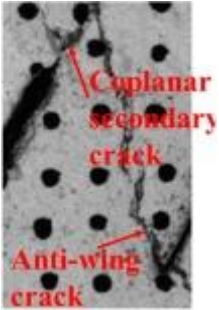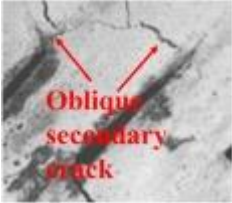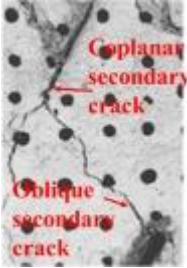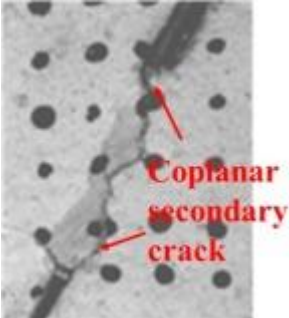Table 7. Coalescence type observed in ductile and brittle specimens.

Ductile specimens	Coalescence types	Brittle specimens	Coalescence types
A1	CSCS-2, CST-3, OSOS-2, TT-3	E1	ATT-1, OST-1, TT-5
A2	TT-4, ATT-1, OSOS-1, CSCS-1, OSCS-1	E2	CSCS-2, OST-1, TT-1
A3	ATT-2, CSCS-1, OST-1	E3	ATT-1, CSCS-1, TT-2
A4	CSCS-1, OSOS-2, TT-2	E4	ATT-3, CSAT-1, CSCS-1, OSOS-1, OST-1, TT-2
B1	ATT-2, CSCS-1, OSOS-1	F1	TT-3, ATT-2
B2	CSCS-2, CST-1, OSOS-2	F2	ATAT-2, CST-1, TT-2
B3	CSCS-2	F3	ATT-1, CSCS-3, OSOS-2, TT-1
B4	ATT-1, ATAT-1, CSCS-2, CST-1	F4	ATAT-1, CSCS-1, TT-5
C1	CSCS-1, CST-1	G1	ATT-2, CSCS-3, TT-3
C2	ATAT-1, ATT-1, CSCS-2, CSAT-1, CST, TT-5	G2	ATT-1, OST-1, CSCS-2, TT-2
C3	CSCS-2	G3	ATAT-4, ATT-1, CSCS-2, TT-3
C4	ATAT-3, ATT-1, TT-3, CST-1	G4	ATAT-2, TT-4
D1	OST-1, CSCS-1	H1	ATT-1, CSCS-2, TT-3
D2	TT-2, CSCS-3, CSAT-1	H2	ATT-2, TT-3

Ductile specimens	Coalescence types	Brittle specimens	Coalescence types
D3	TT-1, CSCS-2	H3	CSCS-1, TT-2
D4	CSCS-2	H4	ATT-4, TT-3

Table 8. Coalescence types in experiments.

Crack coalescence type	Sketch of crack coalescence	Description of crack coalescence type
Type I		Coalescence of two wing cracks (TT)
Type II		Coalescence of wing crack and anti-wing crack (ATT)
Type III		Coalescence of wing crack and oblique secondary crack (OST)
Type IV		Coalescence of wing crack and coplanar secondary crack (CST)
Type V		Coalescence of two anti-wing cracks (ATAT)

| Crack coalescence type	Sketch of crack coalescence	Description of crack coalescence type
Type VI		Coalescence of anti-wing crack and coplanar secondary crack (CSAT)
Type VII		Coalescence of two oblique secondary cracks (OSOS)
Type VIII		Coalescence of coplanar secondary crack and oblique secondary crack (CSOS)
Type IX		Coalescence of two coplanar secondary cracks (CSCS)

In general, for ductile specimens, the coalescence mode is mainly the coalescence of shear cracks, including coalescence types of CSCS, OSOS and OSCS, while for brittle specimens, the coalescence mode is mainly the coalescence of tensile cracks, including coalescence types of TT, ATAT, ATT. The total number of mixed tensile and shear modes of crack coalescence, including coalescence types of CST, CSAT and OST, easily occur when the brittleness index is lower than about 11% in both ductile and brittle specimens, as shown in Table 9. That is to say, the crack coalescence mode transforms from the tensile crack coalescence to mixed tensile and shear crack coalescence, then to shear crack coalescence as the brittleness index decreases.

Table 9. Total number of mixed coalescence mode.

Brittleness index	Mixed coalescence mode	Total number
6.49%	CSAT-1, OST-1	2
6.77%	CST-1, CSAT-1, CST, CST-1	4
9.12%	CST-1, CST-1	2
10.31%	OST-1, OST-1, CSAT-1, OST-1	4
10.85%	CST-3, OST-1,	4
12.22%	CST-1,	1
13.45%	OST-1,	1
15.88%	–	0

4.4. Ultimate failure mode
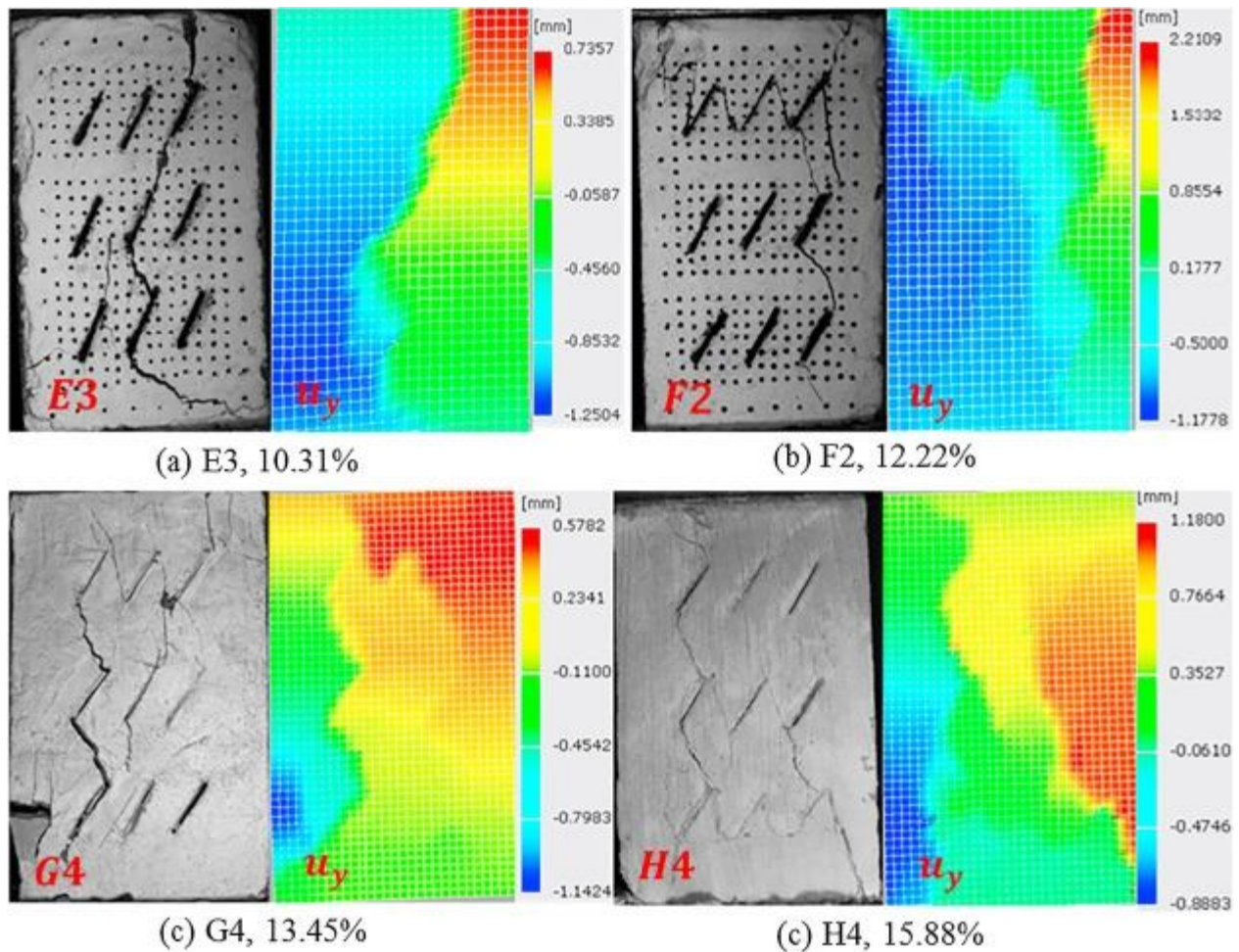
Fig. 20, Fig. 21 show the ultimate failure modes in ductile and brittle rock-like specimens with various brittleness index as well as the corresponding contour of vertical displacement fields. In Fig. 20, Fig. 21, the positive value corresponds to a tensile displacement, and the negative value means a compressive displacement. It can be found from Fig. 20 that the main ultimate failure modes in ductile specimens are shear failure.

(a) D3, 6.49%

(b) C3, 6.77%

(c) B3, 9.12%

(d) A1, 10.85%
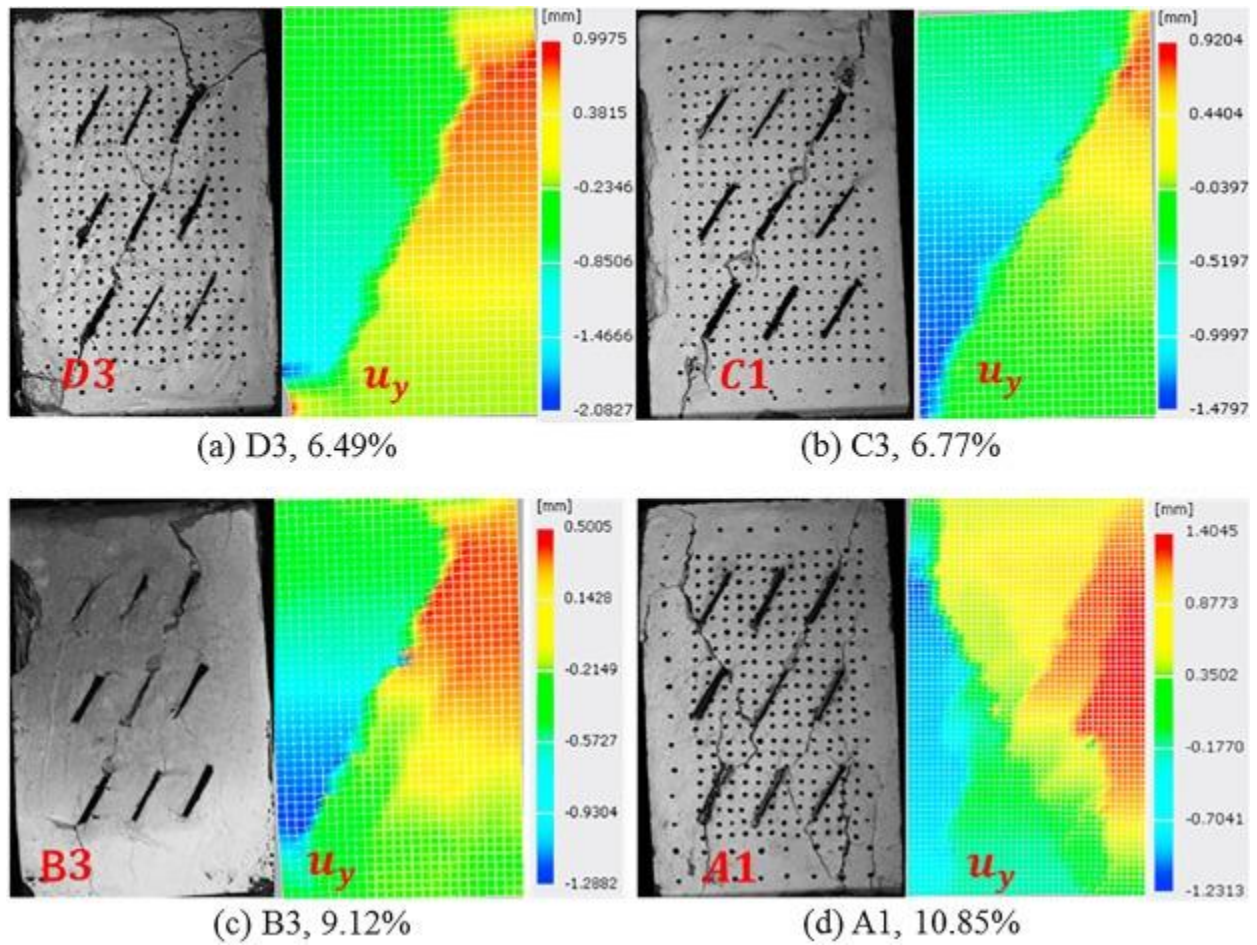
1. Download high-res image (916KB)
2. Download full-size image

Fig. 20. Ultimate failure modes in ductile rock-like specimens.

(a) E3, 10.31%

(b) F2, 12.22%

(c) G4, 13.45%

(c) H4, 15.88%

1. Download high-res image (938KB)
2. Download full-size image

Fig. 21. Ultimate failure modes in brittle rock-like specimens.

In particular, ductile specimens with the brittleness index of 6.49%, 6.77% and 9.12% exhibit pure shear failure induced by a single macroscopic shear crack, as shown in Fig. 20(a), (b) and (c), while ductile specimen with the brittleness index of 10.85% exhibits the mixed tension-shear failure mode, as shown in Fig. 20(d). However, the final failure modes of brittle specimens are quite different from those in ductile rock-like specimens, as shown in Fig. 21. A very interesting phenomenon is that most of crack coalescences occur in a "columnar" pattern, where the flaws on the same column are linked together through the coalescence of two wing cracks in specimens with the brittleness index of 12.22%, 13.45% and 15.88%, as shown in Fig. 21(b), (c) and (d). As a result, tensile macrocracks occur, leading to the splitting failure or tensile failure of brittle specimens. Meanwhile, specimen with the brittleness index of 10.31% exhibits the mixed tension-shear failure mode, as shown in Fig. 21(a). Thus, it can be concluded when the

brittleness index is approximately lower than 9%, ductile specimens exhibit pure shear failure; when the brittleness index is approximately higher than 12%, brittle specimens exhibit pure tensile failure or splitting failure; when the brittleness index varies from 9% to 12%, specimens exhibit the mixed tension-shear failure mode.

Another difference can be found in the contour of vertical displacement field. Fig. 22presents the maximum vertical compressive displacement of specimens in Fig. 20, Fig. 21. For the both of ductile and brittle specimens, the value of the maximum vertical compressive displacement decreases with increasing brittleness index. The main reason is that for ductile rock-like specimens, the strain energy is mainly used in deformations of specimens rather than the cracking behaviors; while for brittle rock-like specimens, more strain energy is mainly used in crack initiation, propagation and coalescence. Therefore, deformation of ductile specimens is larger than that of brittle specimens. The relationship between the maximum vertical compressive displacement and the brittleness index is shown in Fig. 22. The fitting formula can be expressed as follows:

$$(4) \quad y=-4539.6x^3+1579.7x^2-187.4x+8.5234$$

where x is the brittleness index, y is the maximum vertical compressive displacement.
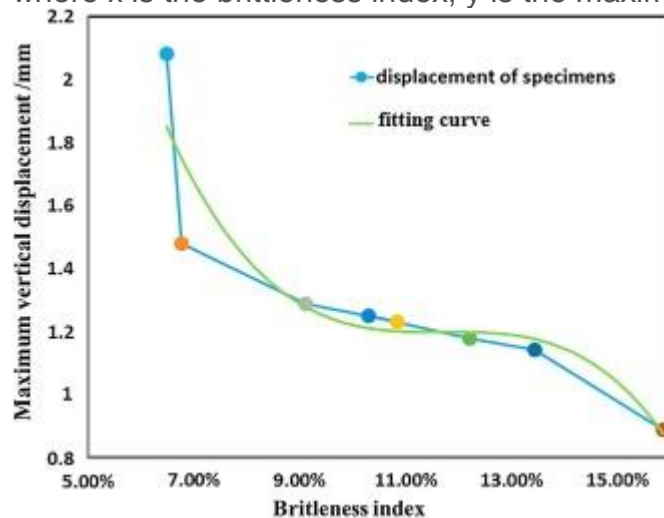
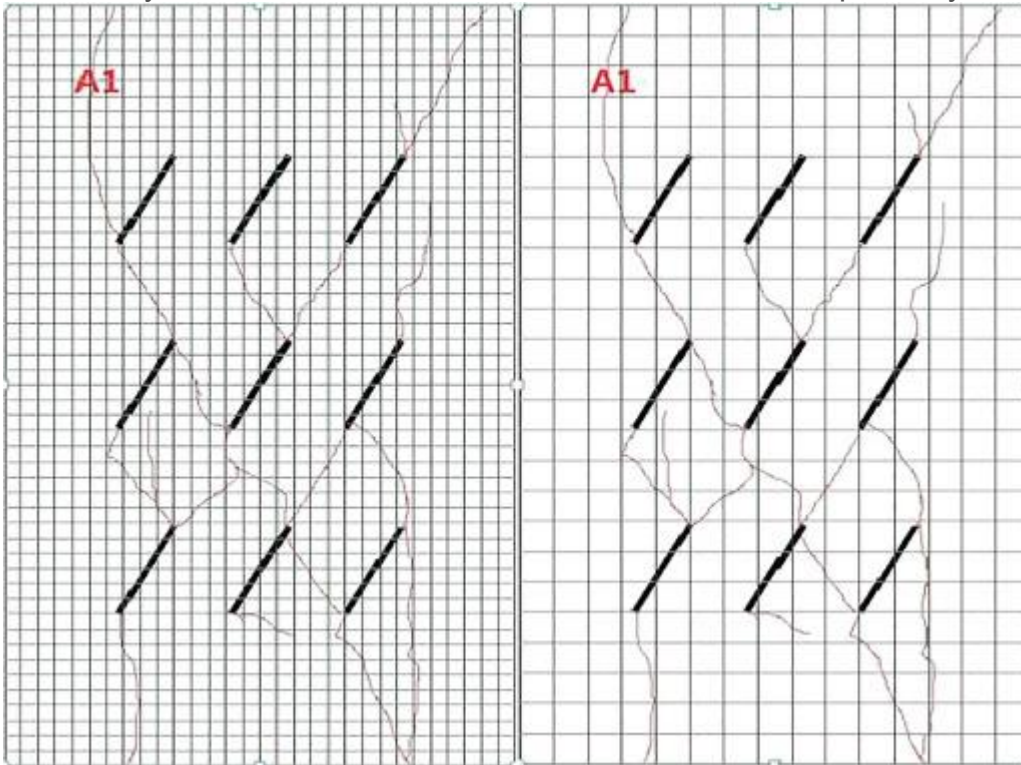1. Download high-res image (104KB)
2. Download full-size image

Fig. 22. Maximum vertical compression displacement of specimens with various brittleness index in ultimate failure state.

5. Fracture process analysis by fractal dimension

In this paper, a box-counting dimension method is applied to calculate the fractal dimension, and a least square method is used to fit the curve of fractal dimension. Taking specimen A1 as a typical example, the calculation process of fractal dimension is described as follows:

(1)

Firstly, meshes with various fractal scales δi = 2 mm, 3 mm, 6 mm, 7.5 mm and 10 mm are applied to cover the fractal body. Fig. 23 only shows specimen A1 covered by meshes with fractal scales 3 mm and 6 mm, respectively.

1. Download high-res image (517KB)
2. Download full-size image

Fig. 23. Meshes with different fractal scale.

(2)

Secondly, the number of grids with different fractal scales covered by cracks in the fractal body is counted, as shown in Table 10.

Table 10. The number of box for specimen A1.

Fractal scale δi/mm	2	3	6	7.5	10
Grids covered by cracks/ N(δi)	232	151	86	62	46

(3)

Thirdly, the least square method is used to fit data listed in Table 10 ($\log\delta_i$-1, $\log(N(\delta_i))$, where $i = 1, 2, 3, 4, 5$. Then, the following equations are written as:

$$(5)\quad y = \alpha_0 + \beta_0 x \quad \alpha_0 = \frac{\sum\log(N(\delta_i))}{n} - \beta_0 \frac{\sum\log\delta_i^{-1}}{n} \quad \beta_0 = \frac{n\sum\log(N(\delta_i))\cdot\log\delta_i^{-1} - \sum\log(N(\delta_i))\sum\log\delta_i^{-1}}{n\sum(\log\delta_i^{-1})^2 - \sum\log\delta_i^{-1}{}^2}$$

where α_0 and β_0 are the fitting parameters, $n = 5$.

(4)

Finally, the fractal dimension can be determined as β_0–value. Then the fractal dimension for specimen A1 is 0.9838.

Investigation of fracture procession of specimens C1, D1, E1 and G1 by fractal dimension methods is shown in Table 11. It can be found that fractal dimension of the specimens increases with increasing damage degree in specimens during the uniaxial compression. This is an expected result because more mesh lattices are covered when more cracks occur in the specimen. It can be concluded that fractal dimension is a reliable method to reveal the damage degree of rocks.

Table 11. Investigation of fracture process by fractal dimension method: (a) specimen B1; (b) specimen D1; (c) specimen E1; (d) specimen G1.

(a)

| Fractal dimension | 0.7768 | 0.9471 | 1.0021 |

(b)

| Fractal dimension | 0.4863 | 0.7983 | 0.9712 |

(c)
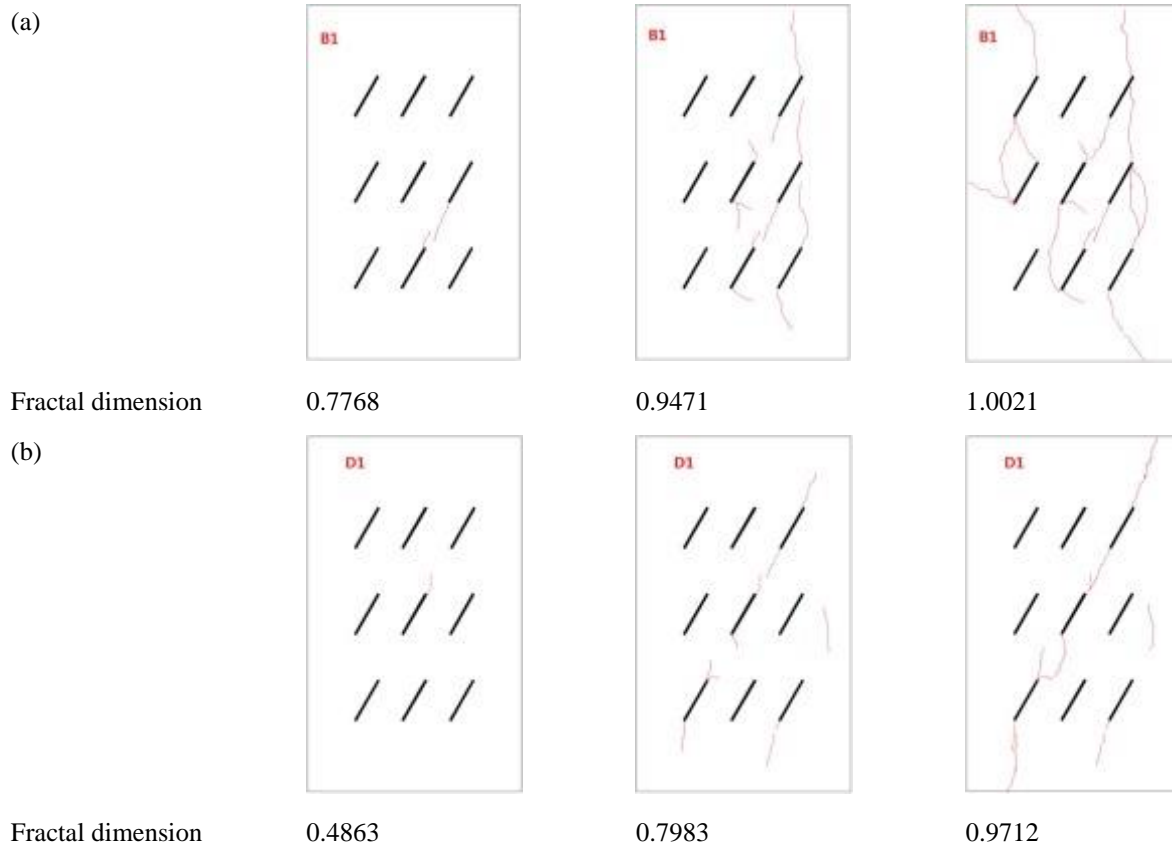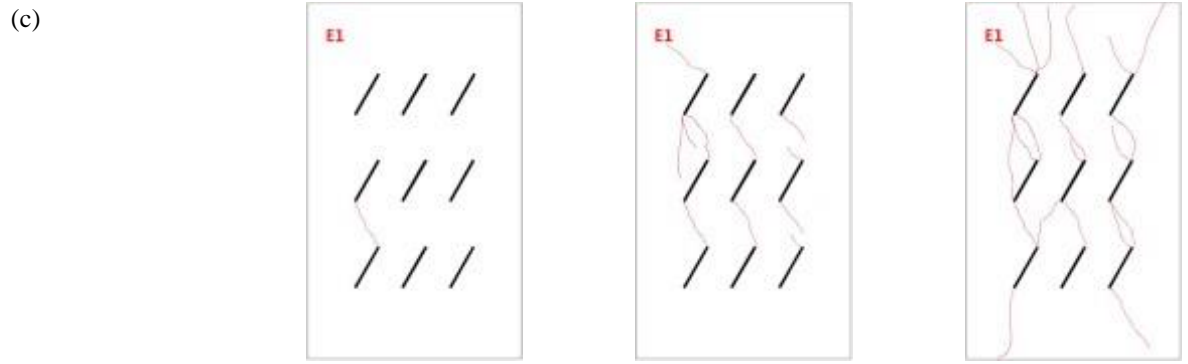
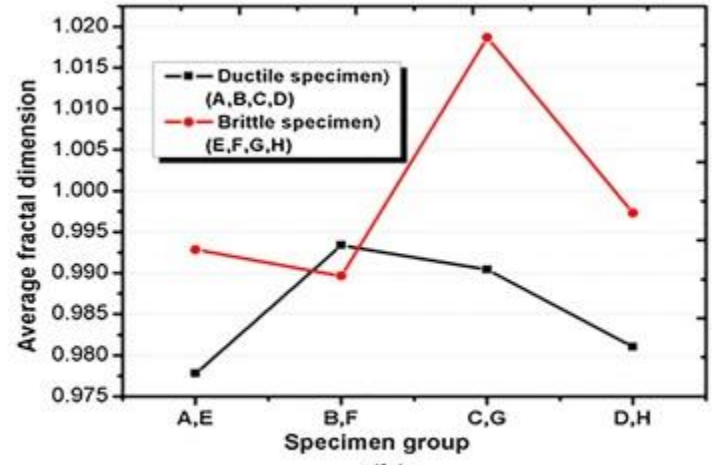| Fractal dimension | 0.8110 | 0.8542 | 1.0079 |

(d)
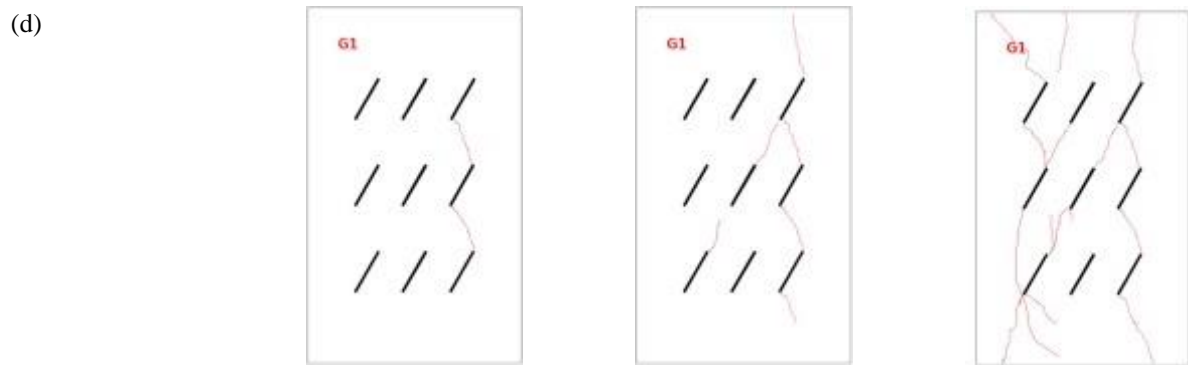
| Fractal dimension | 0.8659 | 0.8915 | 1.1138 |

The fractal dimension of other ductile and brittle specimens in ultimate failure state is plotted in Fig. 24(a). The average fractal dimension of each group of specimens in ultimate failure state is plotted in Fig. 24(b). In general, the larger the brittleness index of materials, the larger fractal dimension in ultimate failure state, as shown in Fig. 24.
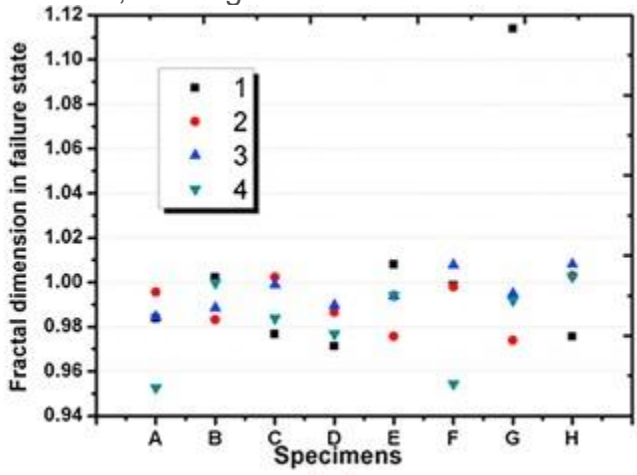
1. Download high-res image (222KB)
2. Download full-size image

Fig. 24. [Fractal dimension](#) of specimens in ultimate failure state: (a) fractal dimension; (b) average fractal dimension.

6. Conclusions

The fracturing behavior of ductile and brittle specimens containing multiple pre-existing flaws under uniaxial compression are investigated by using digital correlation (DIC) technique. Comparisons of [crack initiation](#), propagation and [coalescence](#) between ductile and brittle material have been made. The following conclusions can be drawn:
(1)

For the ductile materials, [peak strength](#) increases with increasing contents of epoxy resin and polyamide, whereas for brittle materials, peak strength increases with increasing the content of colophony. Change in the mass ratio heavily affects the peak strength and the crack initiation stress.
(2)
With the help of two CCD video cameras and digital image correlation technique (DIC), crack initiation, propagation and coalescence process in specimens containing multiple flaws are successfully captured. Contours of strain and displacement fields captured by DIC technique are consistent with the [fracturing processes](#) captured by the CCD cameras. [Crack initiation and propagation](#) can also be detected by the strain concentration in contours of [strain fields](#).
(3)
Nine and eight coalescence types are respectively observed in ductile and brittle rock-like specimens. T coalescence mode more easily occurs in brittle rock-like specimens than in ductile rock-like specimens, while S coalescence mode more easily occurs in ductile rock-like specimens than in brittle rock-like specimens.

(4)
Ultimate failure mode in ductile and brittle material specimens is quite different. Observations on the ultimate failure modes indicate that most macrocracks in brittle multi-flawed rock-like specimens develop from crack coalescence occurring in a "columnar" pattern, while most macrocracks in ductile multi-flawed rock-like specimens develop from shear cracks.

(5)
Wing crack easily occurs in a low ratio of initiation stress to peak strength in the brittle rock-like specimen and splitting failure easily occurs in the brittle rock-like

material, while shear failure mode easily occurs in the ductile specimens, which is the major difference between ductile and brittle rock-like materials.

(6)

A box-counting dimension method is applied to calculate the fractal dimension of new cracks in specimens. Result shows that the fractal dimension of specimens increases with increasing damage degree in specimens; the larger the brittleness index of materials, the larger fractal dimension in ultimate failure state.